

**“Aftereffects” phenomenon in  $^{111}\text{In}$ ( $\rightarrow$  $^{111}\text{Cd}$ )-implanted  $\alpha$ - $\text{Al}_2\text{O}_3$  single crystals: Novel approach integrating experimental double-model analysis with density-functional theory**

G. N. Darriba<sup>a,\*</sup>, R. Vianden<sup>b</sup>, A. P. Ayala<sup>c</sup>, and M. Rentería<sup>a,†</sup>

*<sup>a</sup>Departamento de Física “Prof. Dr. Emil Bose” and Instituto de Física La Plata [IFLP, Consejo Nacional de Investigaciones Científicas y Técnicas (CONICET) La Plata], Facultad de Ciencias Exactas, Universidad Nacional de La Plata, CC 67, (1900) La Plata, Argentina.*

*<sup>b</sup>Helmholtz-Institut für Strahlen- und Kernphysik (HISKP), Universität Bonn, Nussallee 14–16, 53115 Bonn, Germany*

*<sup>c</sup>Departamento de Física, Universidade Federal do Ceará, Fortaleza, CE, 60644-900, Brazil.*

**Abstract.** We develop an experimental double-model analysis, combined with density-functional theory (DFT), to investigate the origin of dynamic hyperfine interactions (HFIs) associated with the electron-capture (EC) decay “aftereffects” (ECAE) phenomenon. This electronic phenomenon, which is reversible with temperature, is typically observed in TDPAC experiments on oxides doped with ( $^{111}\text{In}$ (EC) $\rightarrow$  $^{111}\text{Cd}$ ) probe atoms and was recently explained within an *ab initio* framework based on fluctuations in the number of trapped electron holes at  $^{111}\text{Cd}$  [Phys. Rev. B **105**, 195201 (2022)]. From now on, it is possible to determine, for each measured temperature and observed HFI, the set of *initial* electronic configurations around the probe nucleus and their associated EFGs, whose fluctuations produce these dynamic HFIs, rather than simply identifying the configuration that generates the stable final EFG when the dynamic process ends. We demonstrate the equivalence between the two most used methods for analyzing this type of dynamic HFIs, proposed by Bäverstam *et al.* (BO approach) and Lupascu *et al.* (L approach), successfully connecting the relaxation constant  $\lambda_r$  (the damping strength of the TDPAC spectra) in the BO approach with the distribution's half-width  $\delta_i$  of the initial fluctuating EFGs in the L approach. To address this, we perform a comprehensive DFT study of Cd-doped  $\alpha$ - $\text{Al}_2\text{O}_3$  semiconductor and a detailed *ab initio* analysis of defect-formation energies, both as a function of the Cd impurity's charge state, to unravel controversial TDPAC results reported for  $^{111}\text{In}$ -implanted  $\alpha$ - $\text{Al}_2\text{O}_3$  single crystals, now revisited. From 4 K to 973 K, an unexpected second HFI<sub>d</sub> was observed, and its presence provides essential experimental evidence for demonstrating and quantifying the charge states of the  $^{111}\text{Cd}$  atom during its electronic recovery process. We show that the stable final EFG for the expected undisturbed interaction HFI<sub>u</sub> originates from  $^{111}\text{Cd}$  probes located at defect-free substitutional Al sites (without trapped electron holes) across all measured temperatures. Those of HFI<sub>d</sub> to probes at

Al sites, but with varying amounts of trapped holes after the dynamic process has stopped (ranging from 0 to 0.35, depending on temperature). The lifetime  $\tau_g$  of the holes that are finally ionized (ranging from 5 to 45 ns, depending on the interaction and temperature) provides information about the system's electron availability and mobility. Our integrated analysis shows that one, or at least five, trapped holes are responsible for the dynamic regimes of  $HFI_u$  and  $HFI_d$ , respectively, at intermediate temperatures, when the "aftereffects" are more pronounced. These results quantitatively confirm the physical scenario underlying both the BO and L approaches, and this new method can also be applied to other TDPAC probes without EC. The consolidated proposed scenario also accounts for the observation of well-defined EFGs in ECAE spectra, even when the dynamic regime does not end.

## I. INTRODUCTION

The incorporation of atomic impurities into host lattices can lead to the emergence of new physical properties, as observed, e.g., in semiconducting oxides [1-5]. Experimental techniques such as nuclear solid-state methods, which often use impurity atoms as probes, are essential for investigating local effects at the atomic and sub-nanoscopic levels. The impurity probe serves as an instrument that measures key properties at its site of localization. A powerful tool for studying subtle changes in the electronic structure near probe atoms is the time-differential perturbed  $\gamma$ - $\gamma$  angular correlations (TDPAC) technique. This nuclear spectroscopy measures the hyperfine interaction (HFI) between the nuclear electric quadrupole moment  $Q$  (and/or magnetic dipole moment) of the probe nucleus and the extranuclear electric-field gradient (EFG) tensor (and/or the magnetic hyperfine field) at the probe site, with the ( $^{111}\text{In} \rightarrow$ ) $^{111}\text{Cd}$  nuclide being the most used TDPAC probe. In particular, for electric quadrupole interactions, if a fluctuating EFG (*dynamic* HFI) is sensed by the probe atom rather than the usual *static* EFG, the TDPAC signal exhibits strong time-dependent damping.

In many TDPAC experiments studying  $^{111}\text{In}(\rightarrow)^{111}\text{Cd}$ -doped binary oxides, dynamic HFIs have been observed [6-16]. The electron-capture (EC) decay of the  $^{111}\text{In}$  isotope into the  $^{111}\text{Cd}$  probe atom generates an outward cascade of multiple electron holes through successive Auger processes. If the charge recombination of the latest electron holes (most likely the outermost ones) occurs during the time window of the experimental TDPAC measurement (i.e., between the emission of  $\gamma_1$  and  $\gamma_2$  of the sensitive  $\gamma$ - $\gamma$  cascade of the probe nucleus), a specific type of dynamic HFIs can be detected, a phenomenon known as electron-capture decay *aftereffects* (ECAE). A dynamic regime occurs when charge fluctuations around the probe nucleus induce rapid changes in the EFG magnitude, asymmetry, and/or orientation. Particularly, the ( $^{111}\text{In}(\text{EC}) \rightarrow$ ) $^{111}\text{Cd}$  probe (in a semiconducting or insulating environment) can generate this type of dynamic HFIs on its own, without the need to introduce impurity acceptor or donor levels in the host, as was previously thought. A necessary condition for observing this effect is that the electronic relaxation process exceeds the lifetime of the nuclear state emitting the  $\gamma_1$ -ray that triggers the TDPAC measurement [16]. Experimentally, this effect is characterized by strong damping within the first nanoseconds of the  $R(t)$  TDPAC spectra, followed by a constant reduced anisotropy (the spectrum's amplitude), which is a signature of the end (*switch off*) of the EFG fluctuation (see the naive description of Fig. 2 in Ref. [15]).

Typically, the damping strength decreases reversibly as the measurement temperature (T) increases, completely restoring the anisotropy at higher temperatures.

To analyze this type of  $R(t)$  spectra, the *on-off* perturbation factor proposed by Bäverstam *et al.* [17] (BO approach) and the *unidirectional* electronic relaxation described by Lupascu *et al.* [11] (L approach) are the most commonly used methods in the literature.

In the BO approach [17], the perturbation factor has a straightforward analytical form, which allows the determination of two parameters that characterize the dynamic regime, along with the standard hyperfine quantities related to the final stable  $EFG_f$  tensor: the relaxation constant  $\lambda_r$  (which accounts for the spectrum damping) and the recovery constant  $\lambda_g$ , the inverse of the mean lifetime of the electron holes,  $\tau_g$ , involved in the dynamic process [15]. In this approach, the dynamic parameters  $\lambda_g$  and  $\lambda_r$  can be measured *at each* temperature. However, because of its design, this perturbation factor cannot explicitly provide information about the initial oscillatory EFGs that generate the dynamic behavior.

On the other hand, in the L approach [11], numerical solutions for the perturbation factor are obtained. By comparing these simulations with the experimental  $R(t)$  spectra, the relaxation rate  $\Gamma_r$  to reach a final stable  $EFG_f$  at each measurement temperature can be determined. Within this approach, it is possible to estimate the initial fluctuating EFGs (represented by a mean  $EFG_i$  with a large EFG's distribution half-width  $\delta_i$ ) that relax *unidirectionally* to the final  $EFG_f$  [18]. In this procedure, the distribution of initial EFGs represents the complete set of  $R(t)$  spectra measured at various temperatures, not each spectrum. The  $EFG_f$  is obtained by fitting each spectrum with the standard static perturbation factor, which accurately describes the spectra at longer times. Unlike the BO approach, the L approach does not allow fitting a dynamic perturbation factor to the experimental data; instead, it provides information about the initial oscillating EFG values, which are the same across temperatures.

In recent years, we proposed an *ab initio* scenario compatible with the “aftereffects” phenomenon observed in  $^{111}\text{In}$ -doped tin oxides, identifying the stable electronic configurations that produce the final stable EFGs and constraining the range of fluctuating configurations that drive the dynamic process [15-16]. In these studies, the  $R(t)$  spectra were analyzed solely with the BO approach. We demonstrated that, in these cases, different charge states of the impurity lead to distinct EFGs, which do not always occur across impurity-host systems, suggesting that the system can acquire these charge states during its electronic relaxation. To support this, we performed a comprehensive *ab initio* study of the defect-formation energies for the charge

states of these systems. Our model proposes that rapid random fluctuations among these charge states create fast fluctuating initial EFGs, driving the system into a dynamic regime until it decays to a final stable electronic configuration that produces the EFG observed in this type of TDPAC spectrum. If the initial oscillating EFGs could be determined at each temperature, our *ab initio* EFG calculations would identify which electronic configurations give rise to the dynamic regime, thereby supporting and completing the proposed scenario.

Penner *et al.* [14] reported dynamic hyperfine interactions that exhibit intriguing and controversial behavior when examining the EFG temperature dependence (4-973 K) in  $^{111}\text{In}(\text{EC} \rightarrow ^{111}\text{Cd})$ -doped  $\alpha\text{-Al}_2\text{O}_3$  single crystals. They observed two interactions: HFI<sub>u</sub> (*undisturbed*) and HFI<sub>d</sub> (*disturbed*). HFI<sub>u</sub> denotes  $^{111}\text{Cd}$  atoms occupying single-crystalline Al sites free of structural defects. Conversely, HFI<sub>d</sub> was assigned to  $^{111}\text{Cd}$  atoms occupying Al sites, with randomly distributed structural defects around the probes. Although  $v_Q$  and  $\eta$  values for both HFIs (and their populations) were obtained by fitting a *static* perturbation factor, only HFI<sub>u</sub> was analyzed considering a dynamic behavior within the L approach. HFI<sub>d</sub> was artificially analyzed as a *polycrystalline static* interaction with a wide EFG distribution, although the Cd atoms are located at single-crystalline sites. To elucidate these controversial results, we revisit the experiments using an integrated BO and L approach, along with a comprehensive *ab initio* study of the doped system, thereby obtaining all the information contained in the spectra and clarifying the origin of the “aftereffects” phenomenon.

To achieve these goals, it was first essential to demonstrate the equivalence of the two approaches, identifying  $\lambda_r$  with  $\delta_i$ . Then, applying the BO model to the experiment revisited here enables us to determine the initial fluctuating EFGs that generate the dynamic process for *both* interactions, *independently* at each measurement temperature. The unexpected presence of HFI<sub>d</sub>, rather than being a problem for the analysis of the experimental results, in the present work provides an excellent “laboratory” to demonstrate the existence of different charge states of the  $^{111}\text{Cd}$  probe during the latter stages of the electronic recovery process.

To predict the final stable EFGs observed experimentally and the initial fluctuating ones determined using the double-model approach for both interactions, we perform a thorough density-functional theory (DFT) study of diluted Cd-doped  $\alpha\text{-Al}_2\text{O}_3$  as a function of the impurity’s charge state, employing the Full-Potential Augmented Plane Wave plus local orbitals (FP-APW+lo) method [19]. Additionally, we calculate defect formation energies from first principles for all systems to evaluate the stability of various impurity charge states as final states and the likelihood of fluctuations between specific initial charge states. A comprehensive

analysis of these theoretical results, combined with the integrated experimental analysis, enables us to quantify the electronic configurations (associated with trapped electron holes) that give rise to the initial fluctuating EFGs and the stable final EFGs.

In summary, we introduce a synergistic approach, supported by *ab initio* calculations, that enables analysis of any spectrum exhibiting dynamic hyperfine interactions. This method allows for the extraction of the EFG<sub>f</sub>, the set of EFG<sub>i</sub>, and the electronic configurations - specifically, the number of electron holes - along with their lifetimes. These details offer valuable insights into the electrical properties, such as electron availability and mobility, within the host-impurity system. Additionally, when multiple interactions are present, this approach helps determine whether each interaction is dynamic or static.

This paper is organized as follows. Section II introduces two approaches for analyzing experimental TDPAC spectra with dynamic HFIs produced by the ECAE phenomenon and discusses the conditions required for their equivalence. Section III presents details of *ab initio* electronic structure calculations, including the predicted EFG tensor and defect formation energies for  $\alpha$ -Al<sub>2</sub>O<sub>3</sub>:Cd, considering various Cd charge states. Section IV analyzes the experimental results reported in Ref. [14] using the BO model, providing a synergistic discussion of the integration of the BO and L approaches, their equivalence, and the *ab initio* outcomes. Finally, Section V presents the conclusions.

## II. PERTURBATION FACTORS FOR DYNAMIC HYPERFINE INTERACTIONS

TDPAC spectroscopy enables precise measurement of hyperfine interactions between external electric and magnetic fields and the nuclear quadrupole and/or dipole moments of the intermediate state in a suitable  $\gamma$ - $\gamma$  cascade decay [20-22]. The well-known 171-245 keV  $\gamma_1$ - $\gamma_2$  cascade in the <sup>111</sup>Cd probe nucleus, which results from the EC decay of the <sup>111</sup>In parent, is the most commonly used in this experimental technique. Experimentally, the  $R(t)$  spectrum is built by measuring the number of events (coincidences) where  $\gamma_2$  is detected after a time  $t$  from the  $\gamma_1$  detection (the time window of the TDPAC measurement), at an angle with respect to the direction of  $\gamma_1$ , and can be approximated as:

$$R(t) \cong A_{22}^{\text{exp}} G_{22}^{\text{exp}}(t) , \quad (1)$$

where  $A_{22}^{exp}$  is the experimental anisotropy of the  $\gamma_1$ - $\gamma_2$  cascade and  $G_{22}^{exp}(t)$  is the convolution of the theoretical perturbation factor  $G_{22}(t)$  with the time-resolution curve of the TDPAC spectrometer. The perturbation factor contains all information about the hyperfine interaction and, in our case, the signature of the EFG.

For probes at multiple sites  $j$  in a polycrystalline sample, sensing *static* electric quadrupole hyperfine interactions (i.e., with constant hyperfine parameters during the TDPAC measurement), and spin  $I=+5/2$  of the intermediate nuclear state of the  $\gamma_1$ - $\gamma_2$  cascade,  $G_{22}^s(t)$  is:

$$G_{22}^s(t) = \sum_j f_j \left( S_{20j} + \sum_{n=1}^3 S_{2n_j}(\eta_j) \cos(\omega_{n_j}(\eta_j)t) e^{-\delta_j \omega_{n_j} t} \right) = \sum_j f_j G_{22j}^s(t) , \quad (2)$$

where  $S_{2n}$  and  $\omega_n$  are known functions of the asymmetry parameter  $\eta$  (see Ref. [23] and Ref. [53] therein). The  $\omega_n$  frequencies are proportional to the nuclear quadrupole frequency  $\omega_Q$  through  $\omega_n = g_n(\eta) \omega_Q$ . The exponential factor accounts for a Lorentzian statistical frequency distribution of relative half-width  $\delta$  (in %) around each  $\omega_n$ , distribution reflecting slight differences in the environment of the probes at site  $j$ . For single-crystalline samples, the coefficients  $S_{2n}$  in Ec. (2) also depend on the orientation of the EFG tensor relative to the detectors' coordinate system. Therefore, the spectrum varies with crystal orientation, thereby allowing determination of the EFG tensor's orientation relative to the crystal axes [23].

For a TDPAC probe, as  $^{111}\text{Cd}$ , with spin  $I=+5/2$  and quadrupole moment  $Q$  of the intermediate nuclear state,  $\omega_Q$  is proportional to the largest component of the diagonalized EFG tensor  $V_{33}$  as  $\omega_Q = eQV_{33}/40\hbar$ . Usually, the experimental results are reported using the quadrupole coupling constant  $v_Q = eQV_{33}/\hbar$ . The EFG 2<sup>nd</sup> rank tensor is completely defined by  $V_{33}$  and  $\eta = (V_{11} - V_{22})/V_{33}$ , using the standard convention  $|V_{33}| \geq |V_{22}| \geq |V_{11}|$ .

As mentioned earlier, the most commonly used approaches in the literature for addressing the perturbation factor in dynamic HFIs of the ECAE type are those proposed by Bäverstam *et al.* [17] and Lupascu *et al.* [11]. Both approaches are based on the same premise: the probability that the excited probe atom will decay to a specific final stable electronic state (i.e., unidirectional electronic relaxation) after fluctuations can occur among different charge distributions in the environment of the probe nucleus during the electronic relaxation process (electron hole diffusion inside the atom and electronic recombination). When the system reaches the final stable state, the fluctuating initial EFGs and, consequently, the dynamic HFI are turned off. If this occurs before the TDPAC measurement time window (indicating very fast recombination), a static HFI is observed. Conversely, if this switch-off happens between the  $\gamma_1$

and  $\gamma_2$  coincidence detection, the previously described dynamic  $R(t)$  spectrum with an *on-off* characteristic shape is obtained.

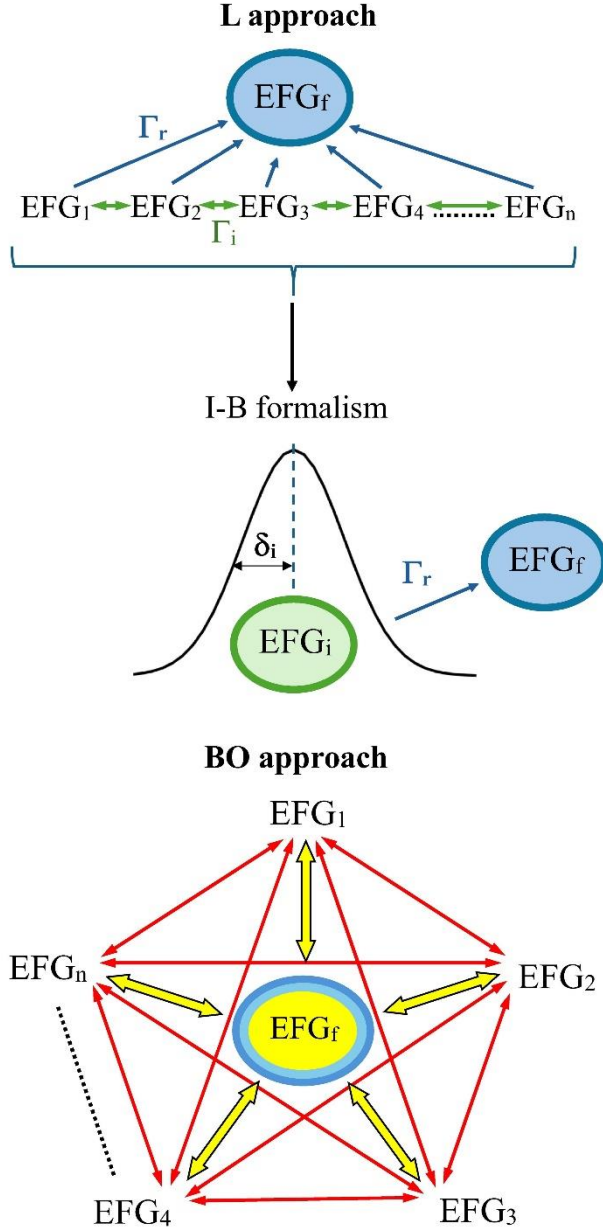


**FIG. 1.** Sketch of different scenarios underlying the construction of the perturbation factors  $G_{22}(t)$  proposed in the Lupascu *et al.* (L) (upper) and Bäverstam *et al.* (BO) (lower) approaches to analyze time-dependent hyperfine interactions caused by electron-capture decay “aftereffects” (ECAE). The L approach includes a simplification based on the Iwatschenko-Borho *et al.* (I-B) formalism (middle). In the L approach,  $\Gamma_r$  is the relaxation rate at which the initial EFGs ( $EFG_n$ ) decay to the final stable EFG ( $EFG_f$ ), after fluctuations among them at rate

$\Gamma_i$ . In the I-B formalism, these fluctuations are replaced by an EFG distribution with a half-width at half-maximum,  $\delta_i$ , centered at a mean EFG value,  $EFG_i$ . In the BO approach, the EFG distribution's half-width of the initial fluctuating EFGs (including also preferentially the most probable EFG<sub>f</sub>) is represented by the relaxation constant  $\lambda_r$ , and the probability of decay to the final stable EFG<sub>f</sub> is defined by the recovery constant  $\lambda_g$  (see text).

### A. The Bäverstam-Othaz (BO) approach

The first approach, proposed by Bäverstam *et al.* [17], is based on the perturbation factor introduced by Abragam and Pound [24] to analyze rapid, random fluctuations in the probe atom's environment in liquid hosts, which produce rapidly varying EFG tensors. This factor has a purely dynamical nature:  $G_{22}^{dyn}(t) = e^{-\lambda_r t}$ . This perturbation factor exponentially reduces the spectrum's anisotropy, and the EFG information is completely lost due to rapid random fluctuations among the EFGs detected by the radioactive probe atoms. In the BO approach for solids, the effect of *fluctuating initial* EFGs during the electronic relaxation of the probe atom is represented by the damping introduced by the relaxation constant  $\lambda_r$ . Additionally, to account for the probability that the excited probe atom decays to a *final stable* electronic state (and thus to a *final stable* EFG,  $EFG_f$ ), BO introduces the atomic recovery constant  $\lambda_g$ , which is the inverse of the mean *lifetime*  $\tau_g$  ( $= \lambda_g^{-1}$ ) of the electron holes, where the lifetime is measured from the emission of  $\gamma_1$ , obtaining:

$$G_{22}(t) = \sum_j f_j \left[ \frac{\lambda_{r_j}}{\lambda_{r_j} + \lambda_{g_j}} e^{-(\lambda_{r_j} + \lambda_{g_j})t} + \frac{\lambda_{g_j}}{\lambda_{r_j} + \lambda_{g_j}} \right] G_{22j}^s(t) \quad , \quad (3)$$

where  $G_{22j}^s(t)$  is the perturbation factor of Eq. (2) describing a *static* HFI at site  $j$ . The detailed construction of these perturbation factors is outlined in Ref [15]. It is important to clarify here that the so-called “electron holes” (mean) lifetime” is an average over the time interval during which the dynamic regime is detected by each <sup>111</sup>Cd atom contributing to each HFI at a certain temperature.  $\tau_g$  actually represents the average lifetime of *only* those electron holes (or fraction of them) that will be finally ionized among all the “dynamic” holes (those involved in the dynamic process) that are trapped at the <sup>111</sup>Cd atom when  $\gamma_1$  is emitted (i.e., when the TDPAC measurement begins). In the case of HFI<sub>u</sub>, *ab initio* calculations will show that the number of “dynamic” and ionized holes is the same; however, this will not be true for HFI<sub>d</sub>. Performing a least-squares fit of Eq. (3) to the experimental  $R(t)$  spectrum enables the determination of the EFG<sub>f</sub> of the final stable state,  $\lambda_g$ , and  $\lambda_r$ . It is important to note that the perturbation factor in

Eq. (3) matches the characteristic shape of the experimental  $R(t)$  spectra where the ECAE phenomenon is observed. An additional benefit of this method is that  $\lambda_g$  and  $\lambda_r$  are free parameters in the fitting process for each observed HFI and at *each* temperature, aligning with the fact that both can vary with temperature as they depend on the host's electron availability and/or mobility [16]. It is interesting to observe that, when electronic decay to a final stable state is absent (without turning *off* the dynamic interaction, i.e.,  $\lambda_g = 0$ ), the perturbation factor simplifies to:

$$G_{22}(t) = \sum_j f_j e^{-\lambda_{rj} t} G_{22j}^S(t). \quad (4)$$

Although a final EFG<sub>f</sub> does not exist in this potential situation, as might occur in an experimental  $R(t)$  spectrum, Eq. (4) still depends on a well-defined EFG through  $G_{22j}^S$ , which would be the EFG<sub>f</sub> when  $\lambda_g$  is small but not null. As proposed in Ref. [25], this observation suggests the existence of a favored population in one of the possible charge states, specifically the lowest-energy state. This indicates a preferential population of one EFG among the initial fluctuating EFGs acting on the probe nucleus during the dynamic process, as shown schematically in the lower part of Fig. 1. When the switching off of the fluctuating process exists ( $\lambda_g \neq 0$ ), as in most of the ECAE cases reported in the literature, the probe atom ultimately decays to this energetically most stable charge state, resulting in the final EFG<sub>f</sub>. The physical implications of this fundamental fact will be discussed and explained in Sec. C after presenting the Lupascu approach.

## B. The Lupascu (L) approach

On the other hand, the L approach develops a comprehensive numerical simulation of the same physical scenario, based on the Winkler-Gerdau model for dynamic HFIs and stochastic processes [26, 27]. The proposed perturbation factor in these simulations (see Eq. (1) of Ref. [11]) models a unidirectional relaxation toward a single final stable EFG<sub>f</sub>, with a relaxation rate  $\Gamma_r$  that depends on temperature. This occurs after fluctuations among a set of arbitrarily chosen initial EFGs (EFG<sub>n</sub>) with a unique fluctuating rate  $\Gamma_i$ . This situation is illustrated in the upper part of Fig. 1. These rapid fluctuations, at least visually, erase information about the initial EFG<sub>n</sub> in the  $R(t)$  spectrum, leaving only the final EFG<sub>f</sub> (as in the BO approach). When fluctuations among the initial EFG<sub>n</sub> are not permitted, the  $R(t)$  spectrum simulation is affected in the first channels, resulting in additional low-intensity EFGs that

conflict with the experimental spectra (see Figs. 4 and 7 in Ref. [28]). In the L approach, comparing simulations with the experimental  $R(t)$  spectra enables determination of  $\Gamma_r$  at each measurement temperature, which is the transition rate to the final stable EFG<sub>f</sub>. This parameter has the same meaning as  $\lambda_g$  in the BO approach. To obtain EFG<sub>f</sub>, a static perturbation factor must be fitted to the “static” part of the spectra, i.e., after the spectrum’s strong dampening has finished. It is important to note here that it is  $\Gamma_r$  (as well as  $\lambda_g$  in the BO approach) that mainly contributes to the characteristic shape of these spectra: the significant decrease of anisotropy in the first nanoseconds and the constant amplitude for longer times (see Fig. 2 in Ref. [15]).

A simplified analytical expression for the perturbation function used in the described simulations can be derived by following the formalism presented by Iwatschenko-Borho *et al.* (I-B) [18], where an initial EFG<sub>i</sub> relaxes unidirectionally to a final EFG<sub>f</sub> with the relaxation rate  $\Gamma_r$  obtained from previous simulations. Both EFG tensors must be *axially symmetric* and share the *same orientation*. However, to account for the fluctuations between different initial EFGs that create the fluctuating regime before relaxing to the final EFG<sub>f</sub>, the L approach models this situation by assuming an extensive EFG distribution with a half-width at half-maximum  $\delta$  centered at a mean initial EFG, EFG<sub>i</sub> (see middle part of Fig. 1), resulting in:

$$G_{22}(t) = \sum_{n=0}^3 S_{2n} \{ [1 - a_n] \cos(n\omega_i t) \exp[-(n\delta_i + \Gamma_r)t] - b_n \sin(n\omega_i t) \exp[-(n\delta_i + \Gamma_r)t] \\ + a_n \cos(n\omega_f t) \exp(-n\delta_f t) + b_n \sin(n\omega_f t) \exp(-n\delta_f t) \} \quad (5)$$

with

$$a_n = \frac{\Gamma_r(\Gamma_r + n\Delta\delta)}{(\Gamma_r + n\Delta\delta)^2 + (n\Delta\omega)^2}, \quad (6)$$

and

$$b_n = \frac{\Gamma_r n \Delta\omega}{(\Gamma_r + n\Delta\delta)^2 + (n\Delta\omega)^2}, \quad (7)$$

where  $\Delta\omega = \omega_f - \omega_i$  and  $\Delta\delta = \delta_i - \delta_f$  [11]. In these equations, EFG<sub>i</sub> and EFG<sub>f</sub> are expressed in terms of  $\omega_{i,f} = 6\omega_{Q_{i,f}}$ .

Equation 5 becomes even simpler when large values of  $\Gamma_r$  are considered, as proposed in the L approach (this condition is necessary to observe a static region in the  $R(t)$  spectra to facilitate the static fit). The *sine* terms can be neglected because, for large  $\Gamma_r$ , the  $b_n$  coefficients approach zero. On the other hand, the factor  $\exp[-(n\delta_i + \Gamma_r)t]$  cancels the first term (which

contains  $\omega_1$ ), only surviving  $G_{22}(t) = S_{20} + \sum_{n=1}^3 S_{2n} a_n \cos(n\omega_f t) \exp(-n\delta_f t)$ , which is (almost) the perturbation factor for a static hyperfine interaction [it only differs in the  $a_n$  coefficient, see Eq. (2)]. At this point, Lupascu *et al.* proposed considering only the dominant term of this summation (which depends on the relative weight of the  $S_{2n}$  coefficients). In the case of polycrystalline samples, as in Ref. [11], the dominant term is  $n=1$ , while in single crystals, as in Penner's experiment [14], it depends on the sample orientation relative to the experimental setup, with  $n=2$  in this case. The other terms can be ignored because the differences they cause are small compared to a complete static perturbation function. In this way, the factor  $A_{22} S_{2n} a_n$  of the dominant term ( $n = 1$  for polycrystals) can be correlated with the amplitude of the static part of the spectra, i.e., with the effective anisotropy of the fitted  $R(t)$  valid for static interactions [see Eq. (1) and Eq. (2)]. In effect, Lupascu *et al.* introduced the *relative amplitude*  $r^j = f_{obs}^j / f^j$  for each inequivalent crystallographic site  $j$ . Here,  $f^j$  denotes the maximum fraction of probes for site  $j$  in the static case (i.e., when the ECAE is completely removed for this site, such as measuring the sample at sufficiently high temperature or on a metallic substrate).  $f_{obs}^j$  is a fraction from  $f^j$ , proportional to the amplitude in the static part of the spectrum observed at each temperature. Then,  $r^j = a_n^j$ , being  $a_n^j$  the factor defined by Eq. (6) corresponding to the dominant  $n\omega_f^j$  frequency in the spectra. In the case of a single crystallographic site ( $f^j=1$ ) in a polycrystalline sample ( $n = 1$  is the dominant term), we have  $r=a_1$  and can directly relate  $f_{obs}$  to  $a_1$ .

In Penner's experiment [14], due to the crystal orientation, we have  $r^u = f_{obs}^u / 1 = a_2$  for HFI<sub>u</sub>, i.e., the dynamic hyperfine interaction whose final EFG<sub>f</sub> is attributed to the *undisturbed* "charge-neutral ground state", which in our *ab initio* scenario corresponds to the impurity level being completely filled (without trapped electron holes). But in that work, Penner *et al.* observed a second hyperfine interaction, the *disturbed* HFI<sub>d</sub>. Since the Penner's spectra in the L approach must be fitted with two *static* HFIs, they had to use a large EFG distribution  $\delta_d$  for the second interaction, assigning it to *structural* defects randomly distributed around the probe. This random, large distribution supports the polycrystalline character proposed to account for HFI<sub>d</sub>, although the sample is single-crystal. Unfortunately, this second interaction was not analyzed using the L approach, which would have enabled us to compare its results with those of the BO approach. To do this, they should also have simulated HFI<sub>d</sub> using another relaxation rate,  $\Gamma_r^d$ , for each temperature and applied the same methodology as for HFI<sub>u</sub>, but with  $r^d = 1 - r^u = f_{obs}^d = a_2^d$ . This can be justified because both interactions are

expected to originate from  $^{111}\text{Cd}$  probes at the same crystallographic site and are highly correlated. Both probe ensembles detect dynamic hyperfine interactions that end at different final EFG<sub>f</sub> values, depending on temperature in the case of HFI<sub>d</sub>. When the “aftereffects” begin to disappear at higher temperatures, HFI<sub>d</sub> feeds HFI<sub>u</sub> and, at the same time, EFG<sub>f</sub><sup>d</sup> tends to match the value of EFG<sub>f</sub><sup>u</sup> (see Fig. 2 in Ref. [14]).

Considering all the mentioned approximations, it is possible to determine the values of  $\Delta\delta$  and  $\Delta\omega$  (see Eq. 6) by fitting  $a_n$  ( $a_1$ ,  $a_2$ , or  $a_3$ ) to the experimental values of  $f_{obs}$  as a function of the previously determined  $\Gamma_r$  the different measuring temperatures, depending on whether the interaction is polycrystalline ( $a_n=a_1$ ) or single crystalline ( $a_n = a_1$ ,  $a_2$ , or  $a_3$ , depending on the crystal orientation). In this form, the average mean value of the initial EFGs, EFG<sub>i</sub>, can be obtained by determining  $\omega_i$  ( $\omega_i = \omega_f - \Delta\omega$ ), and its EFG distribution determining  $\delta_i$  ( $\delta_i = \Delta\delta + \delta_f$ ). Both magnitudes  $\omega_i$  and  $\delta_i$ , related to the initial oscillating EFGs that generate the dynamic interaction, cannot be determined (at least not explicitly) with the BO approach alone.

### C. Equivalence of BO and L perturbation factors

There are some significant differences when applying the L and BO approaches separately to a spectrum. First, the L approach is difficult to use when multiple HFI are present in the spectra, particularly when the sample is single-crystalline. For example, in Penner’s analysis [14], this led to the introduction of a large EFG distribution for HFI<sub>d</sub> in its perturbation factor, justified by structural defects, to compensate for part of the strong damping of the spectra that actually comes from an electronic effect. Second, and critically important, the BO perturbation factor enables, in the presence of multiple interactions, the detection of whether each interaction is dynamic or static (as demonstrated in SnO: $^{111}\text{In}$  [16]). In the L approach, spectra are always fitted with static perturbation factors, even though the hyperfine interactions are dynamic, making it impossible to detect a genuine static component.

It is important to note that although the L and BO approaches are generally regarded as quite different in the literature, it can be shown that, under certain conditions, their perturbation factors match. In this way, this equivalence will enable a novel, synergistic analysis of the dynamic hyperfine interactions observed in TDPAC experiments, supported by first-principles electronic structure calculations.

To show this, let us consider a single dynamic hyperfine interaction for simplicity. The first approximation is to assume that the mean of the initial fluctuating EFGs, denoted by  $\omega_i$  in

the L approach, is very similar to the final EFG<sub>f</sub>, associated with  $\omega_f$ . In this case,  $\Delta\omega$  can be neglected and the  $b_n$  coefficients vanish [see Eq. (7)], removing the *sine* terms in Eq. (5). The second approximation is to take  $n\Delta\delta \rightarrow \Delta\delta$ . This assumption closely resembles the simplification used in the L approach, which ultimately considers only the dominant  $n = 1$  term in Eq. (5) due to the significant value of  $S_{21}$  (in polycrystalline samples). Hence, both approximations ( $n\Delta\delta \rightarrow \Delta\delta$  and  $\omega_i \approx \omega_f$ ) applied to Eq. (5) make the coefficient  $a_n$  independent of  $n$  and allow it to be factored out of the summation. This is a general result valid for all values of  $\Gamma_r$ . In effect, the condition of large  $\Gamma_r$  values mentioned in Sec. II. B was used solely to simplify Eq. (5) and facilitate the static fit needed within the L approach. This section aims to show the conditions under which the BO approach and the IB proposal in Eq. (5) are equivalent, avoiding any unnecessary approximations used earlier in the L approach.

With these two approximations, Eq. (5) is reduced to:

$$\begin{aligned} G_{22}(t) &= \left\{ \frac{\Delta\delta}{\Gamma_r + \Delta\delta} \exp[-(\Delta\delta + \Gamma_r)t] + \frac{\Gamma_r}{\Gamma_r + \Delta\delta} \right\} \sum_{n=0}^3 S_{2n} \cos(n\omega_f t) \exp(-n\delta_f t) = \\ &= \left\{ \frac{\Delta\delta}{\Gamma_r + \Delta\delta} \exp[-(\Delta\delta + \Gamma_r)t] + \frac{\Gamma_r}{\Gamma_r + \Delta\delta} \right\} G_{22}^s(t) \end{aligned} \quad (8)$$

Comparing Eq. (8) with Eq. (3) (just for a single site), we see that both perturbation factors coincide if the relaxation rate  $\Gamma_r$  and  $\Delta\delta$  ( $\Delta\delta = \delta_i$ , since  $\delta_f$  is really very small) of the L approach are associated with the recovery constant  $\lambda_g$  and the relaxation constant  $\lambda_r$  of the BO approach, respectively.

We note here the importance of this equivalence. By combining the two approaches, it is possible to determine the range of initial EFGs that generate the dynamic interaction and the lifetimes of the electron holes involved in the relaxation process for each measured temperature and each observed hyperfine interaction. Within this framework of equivalence, BO directly provides the half-width of the EFG distribution in the dynamic regime at each temperature (via  $\lambda_r$ ). Since  $\omega_i \approx \omega_f$ , and  $\omega_f$  is experimentally determined, the BO approach can also provide a reasonably accurate estimate of the mean EFG<sub>i</sub> and its distribution half-width, now for *each temperature*. In turn, the L approach allows determination of the central value of the EFG distribution, EFG<sub>i</sub>, but it is an average over all measurement temperatures.

After this analysis, it is essential to note that when the results of the L approach in a specific case or experiment confirm the conditions necessary for the equivalence between the two perturbation factors (Eqs. 3 and 5), namely  $\omega_i \approx \omega_f$ , our proposal underlying the BO

approach is validated since the final  $EFG_f$  is among the initial fluctuating  $EFGs$  and has the highest probability. In Sec. IV, we will demonstrate that the conditions required for the equivalence are satisfied for the case of  $\text{Al}_2\text{O}_3:(^{111}\text{In} \rightarrow)^{111}\text{Cd}$ , after our integrated analysis is completed.

### III. AB INITIO CALCULATIONS

#### A. Calculation details

To obtain a highly accurate description of the electronic density  $\rho(\mathbf{r})$ , we performed *ab initio* DFT electronic structure calculations for the Cd-doped  $\alpha$ - $\text{Al}_2\text{O}_3$  semiconductor (*corundum* crystal structure). We use the hexagonal representation of its unit cell, which contains three rhombohedral primitive cells (space group  $R\bar{3}c$ ), as shown in Fig. 2. In this representation, the structure has  $a = b = 4.75999(3)$  Å and  $c = 12.99481(7)$  Å [29], with 12 Al and 18 O atoms at  $\pm(0, 0, u)$ ;  $\pm(0, 0, u+1/2)$ ;  $rh$  and  $\pm(v, 0, 1/4)$ ;  $\pm(0, v, 1/4)$ ;  $\pm(-v, -v, 1/4)$ ;  $rh$  positions, respectively, where  $u = 0.35219(1)$  and  $v = 0.30633(5)$ . The “ $rh$ ” term implies adding  $(1/3, 2/3, 2/3)$  and  $(2/3, 1/3, 1/3)$  to the previous coordinates. In this oxide, each Al atom has six nearest oxygen neighbors (ONN), three (O1) at 1.854 Å and three (O2) at 1.972 Å.

To simulate the condition of diluted impurity, where each impurity does not interact with its nearest images and the structural relaxation caused by the impurity in its neighbors does not influence the relaxations induced by the closest impurities, we replace one of the 12 Al atoms with a Cd atom [Fig. 2(b)], as shown to be sufficient for this doped system [30]. The diluted-impurity condition is essential for accurately comparing *ab initio* calculations with TDPAC experiments, where the impurity probe atom is highly diluted (at the ppm level).

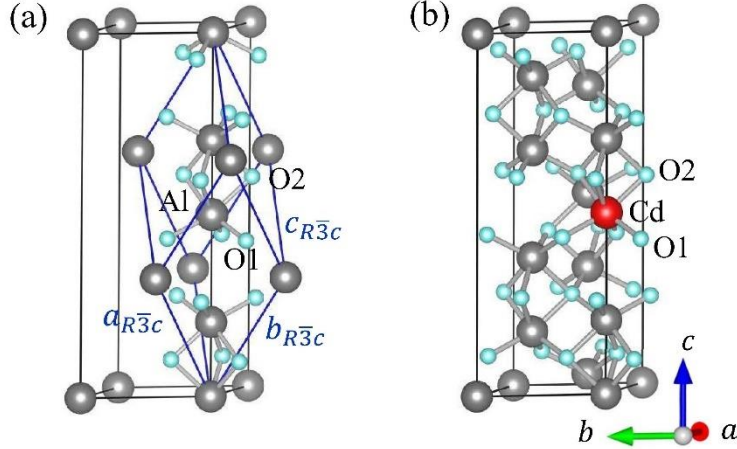


**FIG. 2.** (a) Rhombohedral  $\alpha$ -Al<sub>2</sub>O<sub>3</sub> primitive cell. Gray and light blue spheres indicate Al and O atoms, respectively. (b) Cd-doped  $\alpha$ -Al<sub>2</sub>O<sub>3</sub> hexagonal unit cell used in all calculations, with one Al atom replaced by a Cd impurity (red sphere).

Once an Al atom is replaced by a Cd atom (calling this system Al<sub>2</sub>O<sub>3</sub>:Cd<sup>0</sup>), we performed calculations for various charge states of the doped system. Since an electronic recombination process occurs around the <sup>111</sup>Cd impurity in the actual samples, and considering the nominal acceptor nature of Cd<sup>2+</sup> when it replaces Al<sup>3+</sup> in the  $\alpha$ -Al<sub>2</sub>O<sub>3</sub> host, we add electronic charge to the Al<sub>2</sub>O<sub>3</sub>:Cd<sup>0</sup> system in 0.05 e<sup>-</sup> steps up to 1 e<sup>-</sup>, calling it Al<sub>2</sub>O<sub>3</sub>:Cd<sup>x-</sup> for the doped system where an amount of  $x$  electrons is added, leaving it in a  $q=x-$  charge state. On the other hand, to account for thermal effects on the structural parameters of  $\alpha$ -Al<sub>2</sub>O<sub>3</sub>, we use experimental lattice parameters as a function of temperature [31].

The FP-APW+lo method [19], implemented in the WIEN2k code [32], was used. For all calculations, we set a cutoff parameter for the plane-wave basis  $R_{MT}K_{\max} = 7$ , where  $K_{\max}$  is the largest magnitude of the reciprocal lattice vectors, and  $R_{MT}$  is the smallest radius of the non-overlapping muffin-tin spheres. The radii of the spheres centered on the Cd, Al, and O atoms were  $R_{MT}(\text{Cd}) = 1.06$  Å,  $R_{MT}(\text{Al}) = 0.87$  Å, and  $R_{MT}(\text{O}) = 0.85$  Å, respectively. The integration in reciprocal space was performed using the tetrahedron method [33], with a  $k$ -space grid of 9x9x2. The Perdew-Burke-Ernzerhof (PBE-GGA) parametrization [34] was employed to treat exchange and correlation. Finally, to determine the equilibrium structures, a Newton-damped scheme was used until the forces on the ions dropped below 0.01 eV/Å, and the EFG tensors were calculated from the second derivative of the full electric potential obtained for the final equilibrium structures [35, 36].

## B. *Ab initio* results and the origin of dynamic hyperfine interactions

Replacing an Al atom with a Cd impurity in the  $\alpha$ -Al<sub>2</sub>O<sub>3</sub> system (Al<sub>2</sub>O<sub>3</sub>:Cd<sup>0</sup>) causes significant forces on its nearest oxygen neighbors. Therefore, to find the equilibrium structure, all atomic displacements in the cell were allowed in our calculations. As shown in Ref. [30], the presence of the Cd impurity results in outward relaxations of O1 and O2, increasing the bond lengths dCd-O1 and dCd-O2 by 11% and 14 %, respectively. Furthermore, the Cd impurity introduces an atomic impurity level into the electronic density of states (DOS) within the energy band gap of pure  $\alpha$ -Al<sub>2</sub>O<sub>3</sub> semiconductor, near the top of the valence band (TVB), as shown in Fig. 3. This impurity level mainly consists of Cd-4d, Cd-5p, and O-2p states. It is partially filled, with unoccupied states corresponding to one electron, consistent with the nominal acceptor character of Cd<sup>2+</sup> substituting Al<sup>3+</sup>. In this context, adding electronic charge to the Al<sub>2</sub>O<sub>3</sub>:Cd<sup>0</sup> system causes the impurity level's empty states to begin filling—in other words, the Fermi level shifts to the right in a band rigid model—until one electron is added, resulting in Al<sub>2</sub>O<sub>3</sub>:Cd<sup>1-</sup>, which fills the impurity level. Although the calculation adds the charge to the doped system, we sometimes refer to this as the “impurity's charge state” since the extra charge mainly localizes at the Cd atom (consistent with the atom-projected partial DOS [30]) and much less at its ONN, as Fig. 4 shows. This electron density  $\rho(\mathbf{r})$  is a “snapshot” of the added electron [projected on the (010) plane] that fills the impurity level.

When the charged systems reach their new equilibrium atomic positions, dCd-O1 remains essentially unchanged, while dCd-O2 increases (outward relaxation). In *all* cases, the predicted EFG has axial symmetry ( $\eta = 0$ ), and the direction of  $V_{33}$  stays along the [001] crystalline axis. This previously unknown information about the EFG tensors for different charge states of the <sup>111</sup>Cd probe will be crucial for validating the requirement, within the L approach, that the initial and final EFGs must have *the same orientation and axial symmetry*, as needed by the I-B formalism [18].

Figure 5 compares the *ab initio* predictions of  $V_{33}$  with the experimental results obtained by Penner *et al.* [14]. The dashed areas indicate the range of  $V_{33}$  values for each interaction across the entire measured temperature range.

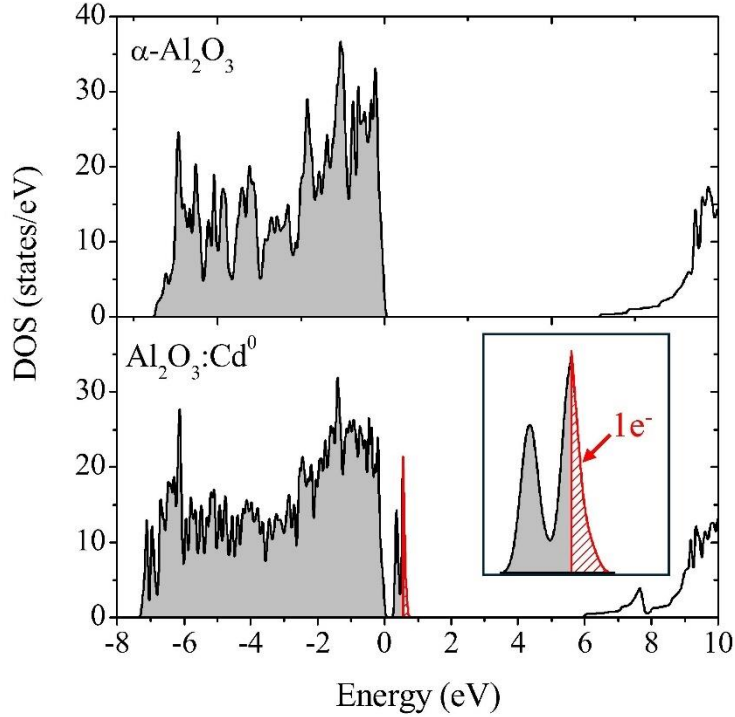


**FIG. 3.** Total electronic density of states (DOS) for pure (top) and Cd-doped (bottom)  $\alpha$ -Al<sub>2</sub>O<sub>3</sub> (Al<sub>2</sub>O<sub>3</sub>:Cd<sup>0</sup>). The gray areas indicate occupied states. A zoom-in on the Cd impurity level is included. The dashed red region highlights the acceptor level introduced by the Cd impurity.

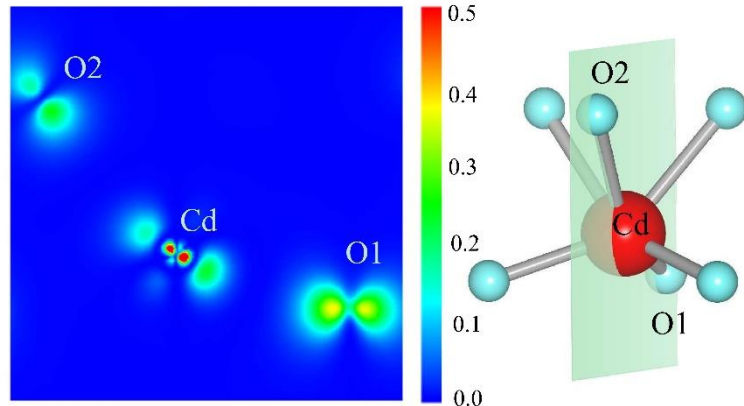


**FIG. 4.** Electron density  $\rho(\mathbf{r})$  in the Al<sub>2</sub>O<sub>3</sub>:Cd<sup>1-</sup> system corresponding to the energy range of the added electron in the DOS, projected onto the (010) plane. The right side shows the Cd-O1 and Cd-O2 bonds belonging to this plane.

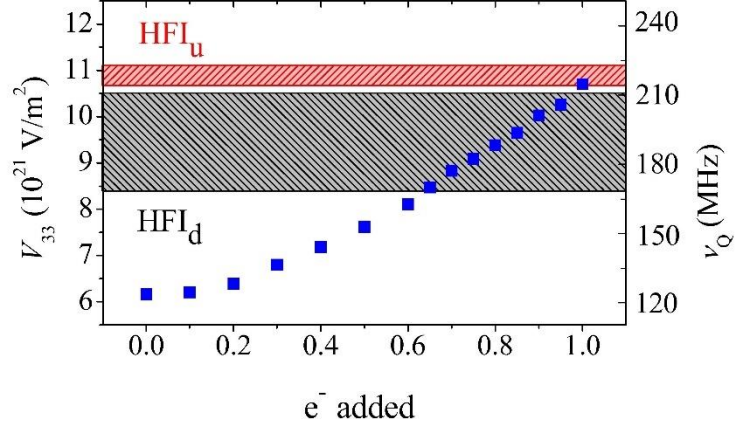


**FIG. 5.** Predicted  $V_{33}$  at the Cd site in  $\text{Al}_2\text{O}_3:\text{Cd}^{x-}$  as a function of added electrons to the system (blue squares), using lattice parameters at room temperature. The dashed areas indicate the experimental values of  $\text{HFI}_u$  (red) and  $\text{HFI}_d$  (gray) in the 4-973 K measurement temperature range. To obtain  $V_{33}$  from  $v_Q$ , we used  $Q = +0.83(13)$  b [37].

Figure 5 shows that  $\text{HFI}_u$  can be associated with  $^{111}\text{Cd}$  probes located at substitutional Al sites free of defects, with the impurity level fully occupied ( $\text{Al}_2\text{O}_3:\text{Cd}^{1-}$  system), indicating the absence of trapped electron holes. The duplication of  $V_{33}$  when an electron is added to the  $\text{Al}_2\text{O}_3:\text{Cd}^0$  system, which ionizes the electron hole mainly trapped at the Cd atom, can be qualitatively explained by examining the electronic density  $\rho(\mathbf{r})$  shown in Fig. 4. This change in the EFG results from the modification of  $\rho(\mathbf{r})$  inside the muffin-tin sphere around Cd, especially near the Cd nucleus. To analyze this change, we consider how the magnitude and sign of  $V_{33}$  depend on the angle between a negative charge distribution and the  $V_{33}$  direction (as described by Eq. (14) in Ref. [15]). Negative charges at angles less than  $54.7^\circ$  from the  $V_{33}$  direction (parallel to the [001] crystal axis), shown as the red spot on the left side of the Cd atom in Fig. 4, contribute negatively to  $V_{33}$ . Those closer to the (001) plane (at an angle less than  $35.3^\circ$  from this plane) contribute positively, as does the larger red spot to the right of Cd. The greater accumulation of negative charge at the Cd site closer to the (001) plane accounts for the notable increase in EFG as negative charge is added to the system.

Penner's results show that the reported  $V_{33}$  value for  $\text{HFI}_u$  is not constant, decreasing slightly as  $T$  increases [14]. To understand this temperature dependence, we performed calculations in the  $\text{Al}_2\text{O}_3:\text{Cd}^{1-}$  system, using experimental lattice parameters that change with temperature [31]. The strong agreement between the experimental data and our calculations of the  $V_{33}$  temperature dependence (see Fig. 6) indicates that this behavior arises from thermal lattice expansion rather than electronic effects. Notably, the significant nonlinear expansion of

the  $a$  and  $c$  lattice parameters with increasing temperature [31], as used in the calculations, explains the slight linear dependence of  $V_{33}$  observed.

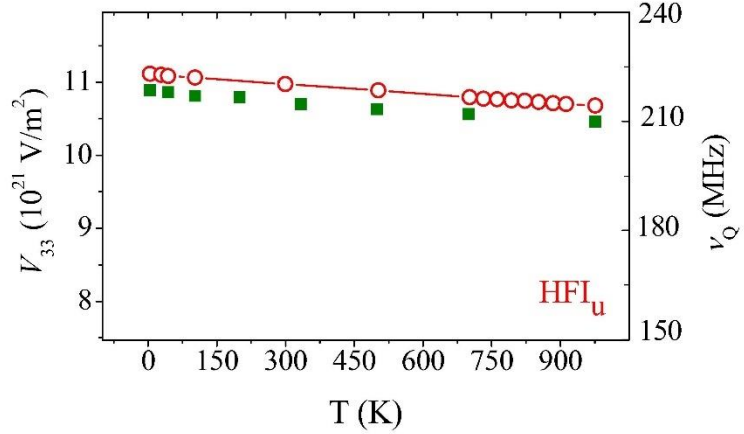


**FIG. 6.** Comparison of predicted  $V_{33}$  for  $\text{Al}_2\text{O}_3:\text{Cd}^{1-}$  (green squares) using the experimental lattice parameter as a function of temperature with the experimental  $V_{33}$  values of HFI<sub>u</sub> (open red circles) reported by Penner *et al.* [14].

Conversely, as demonstrated by the *ab initio* EFG calculations, HFI<sub>d</sub> can be connected to  $^{111}\text{Cd}$  probes at substitutional Al sites. Still, the final stable electronic environments (i.e., charge states) vary with temperature. In fact, both Fig. 5 and Fig. 7 show that the  $V_{33}$  values of HFI<sub>d</sub> as a function of temperature match very well with the  $V_{33}$  predictions within the range of 0.65 to 1 electron added to the doped system (corresponding to 0.35 to 0 trapped holes at the  $^{111}\text{Cd}$  atom when recombination ends). Figure 7 also demonstrates that the complete electronic recovery of the  $^{111}\text{Cd}$  atom (filled impurity level) occurs at very high and very low temperatures, where HFI<sub>d</sub> converges, not by chance, to the value of HFI<sub>u</sub>.

But why might these specific EFGs of HFI<sub>d</sub> have been observed in the experiment? Let's analyze the defect-formation energy study of a Cd impurity in  $\alpha$ - $\text{Al}_2\text{O}_3$  as a function of its charge state.

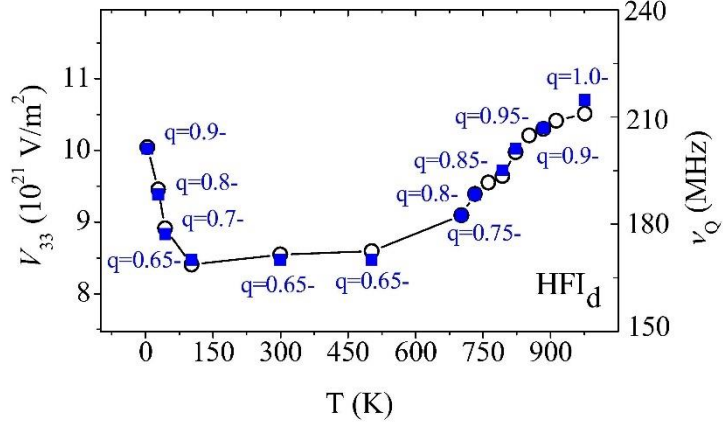


**FIG. 7.** Comparison of predicted  $V_{33}$ , based on the impurity's charge state and lattice parameters at RT (blue squares), with the experimental  $V_{33}$  values of  $HFI_d$  (open circles) reported by Penner *et al.* [14] as a function of temperature.

For the Cd-doped  $\alpha$ -Al<sub>2</sub>O<sub>3</sub> system, the defect formation energy in a charge state  $q$  is:

$$E_f(\text{Al}_2\text{O}_3:\text{Cd})^q = E^q(n_{Al}, n_O, n_{Cd}) - n_{Al}\mu_{Al} - n_O\mu_O - n_{Cd}\mu_{Cd} + q(\varepsilon_F + \varepsilon'_v) \quad . \quad (9)$$

Here,  $E^q(n_{Al}, n_O, n_{Cd})$  is the total energy of the Cd-doped  $\alpha$ -Al<sub>2</sub>O<sub>3</sub> system in the charge state  $q$ , with  $n_{Al}$ ,  $n_O$ , and  $n_{Cd}$  atoms of aluminum, oxygen, and cadmium, being their chemical potentials  $\mu_{Al}$ ,  $\mu_O$ , and  $\mu_{Cd}$ , respectively.  $\varepsilon_F$  is the Fermi energy, relative to the energy of the top of the valence band of the doped system,  $\varepsilon'_v$ .  $\varepsilon_F$  takes values between 0 and the band gap energy  $\varepsilon_g$  ( $0 \leq \varepsilon_F \leq \varepsilon_g$ ). Following the formalism developed in Ref. [30], we have:

$$E_f(\text{Al}_2\text{O}_3:\text{Cd})^q = E(\text{Al}_2\text{O}_3:\text{Cd})^q - E(\text{Al}_2\text{O}_3) + \mu_{Al}^* + \frac{1}{2}\Delta_f H^{\text{Al}_2\text{O}_3} - \mu_{Cd}^* - \Delta_f H^{\text{Cd}0} + q(\varepsilon_F + \varepsilon'_v) \quad (10)$$

where  $\mu_x^*$  is the total energy per atom of the metallic crystal  $x$ , and  $\Delta_f H^Y$  is the formation enthalpy of the compound  $Y$ . Figure 8 shows the results for the defect formation energy across all studied charge states, from 0 to 1 electron hole at the Cd atom. This corresponds to the Al<sub>2</sub>O<sub>3</sub>:Cd<sup>1-</sup> and Al<sub>2</sub>O<sub>3</sub>:Cd<sup>0</sup> systems (red lines). It also displays the result of adding 1.1 e-, which is 0.1 e- more than in the system with the impurity level filled (dash blue line), and with two

electron holes, meaning one electron removed from the  $\text{Al}_2\text{O}_3:\text{Cd}^0$  system (green line). These results indicate that adding more electrons when the impurity level is filled is energetically less favorable, as well as the existence of two electron holes trapped at the Cd atom (unless the Fermi energy  $\varepsilon_F$  is very close to the top of the VB or in deeper states).

As shown, in an acceptor case such as the current impurity-host system, the charge state corresponding to the fully occupied impurity level ( $q=1^-$ ) has the lowest energy over a wide range of the Fermi energy [see Fig. 8(a)]. However, when an EC creates the probe atom, subsequent Auger processes generate many electron holes that diffuse to the outer shells of the atom (within about  $10^{-14}$  s), leaving it highly ionized. These holes are then filled based on the behavior of the defect formation energy. Because the initial stage of the electronic recovery of the Cd atom – where electrons from neighboring ions fill the holes – is very fast (about  $10^{-12}$  s), only the most recent electron holes in the outermost shells can eventually be detected in a TDPAC experiment. These may produce either a dynamic or a static HFI, depending on the electrical properties (metallic, semiconducting, or insulating) of the host and the lifetime of the nuclear level that emits  $\gamma_1$  [16].

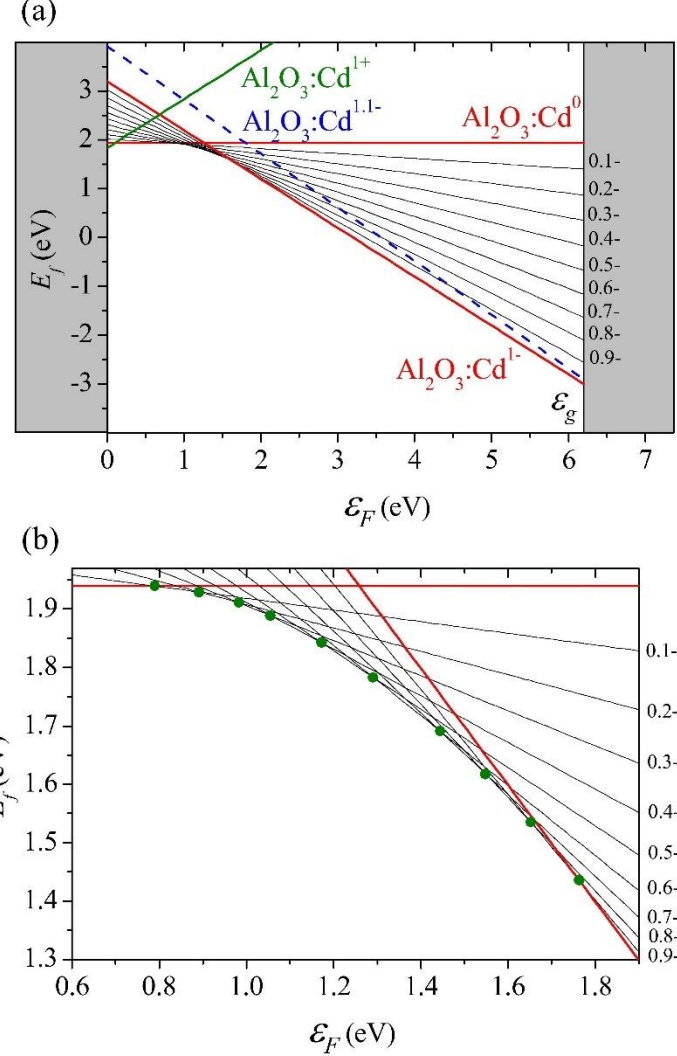


**FIG. 8.** (a) Defect formation energy  $E_f$  as a function of Fermi energy  $\epsilon_F$  for all studied  $\text{Al}_2\text{O}_3:\text{Cd}^q$  systems. Red lines correspond to  $q=1-$  and  $q=0$ , while black lines depict  $q=0.1-$ ,  $0.2-$ ,  $0.3-$ ,  $0.4-$ ,  $0.5-$ ,  $0.6-$ ,  $0.7-$ ,  $0.8-$ , and  $0.9-$ . Results for  $q=1.1-$  (dash blue line) and  $q=1+$  (green line) are also shown. The gray energy regions below 0 eV and above  $\epsilon_g$  represent the valence and conduction bands, respectively, as predicted for pure  $\alpha\text{-Al}_2\text{O}_3$ . (b) Zoomed-in view of the band gap energy region with  $\epsilon_F$  between 0.6 and 1.9 eV, where lines for  $q=n$  and  $q=n+0.1$  intersect.

Taking all this into account, it is now clear where HFI<sub>u</sub> originates. Its EFG value matches the EFG prediction for  $\text{Al}_2\text{O}_3:\text{Cd}^{1-}$ , indicating it represents  $^{111}\text{Cd}$  atoms located at structural-defect-free cation sites. These atoms, after experiencing different fluctuating electronic environments caused by shifts during the filling of the last Cd electronic empty states, decay to the stable charge state that corresponds to the impurity level being fully filled.

Inspecting Fig. 8 (a) and then Fig. 8 (b) for greater accuracy, we observe that systems with charge states between  $q=0$  and  $q=1-$  (with different predicted EFGs) have very similar formation energies when the Fermi energy is around  $\varepsilon_F = 1.25$  eV; the same applies for  $q=0$  and  $q=1+$  near the TVB, supporting the idea of random fluctuations in this charge state range and, consequently, between their EFGs. These fluctuations are necessary in all approaches proposed to date for describing the ECAE phenomenon and constructing their perturbation factors, as previously described.

Now, let's analyze the origin of  $\text{HFI}_d$ . The previous situation can be slightly altered if the “reservoir of electrons” in the current sample—generally related to the host's electronic properties, the balance between intrinsic donor and acceptor impurities, the increase in electron availability due to thermal effects at higher temperatures, and, as seen in this case, electron conductivity at very low temperatures—decreases the Fermi energy to below approximately 1.8 eV. The ECAE process favors this change and is temperature-dependent. Figure 8(b) demonstrates that as the Fermi energy drops, charge states with a greater proportion of electron holes possess the lowest energy. The final EFGs observed by  $\text{HFI}_d$  as a function of temperature match perfectly with  $^{111}\text{Cd}$  atoms decaying to a final stable charge state, ranging from 0.65 to 1 added electron (see Fig. 5). This corresponds to a Fermi energy range of approximately 1.5 to 1.8 eV, across the entire measurement temperature range [see Fig. 8 (b)]. In Fig. 7, the temperature dependence of the Fermi energy can be deduced, confirming the final stable charge states reached by the  $^{111}\text{Cd}$  atom. In effect, the lower Fermi energy value ( $\varepsilon_F = 1.5$  eV and  $q=0.65-$ ) aligns with the very high population observed for  $\text{HFI}_d$  in Ref. [14], between approximately 75 and 500 K, indicating that there are not enough electrons to fully fill the impurity level for almost all the  $^{111}\text{Cd}$  probes due to the additional electron holes created by the EC and the low electron availability at these temperatures. It is important to note that in TDPAC experiments on  $\alpha\text{-Al}_2\text{O}_3$  single crystals implanted with  $^{111m}\text{Cd}^+$  ions, a *single static* HFI was observed (between 77 and 873 K) with the same EFG of  $\text{HFI}_u$  [13]. In these experiments [13], the same sensitive nuclear state of  $^{111}\text{Cd}$  is used to measure the HFI. However, this state is populated from the  $11/2^+$  isomeric state (with a very long lifetime of 48.6 minutes) of  $^{111m}\text{Cd}$  through a 151 keV  $\gamma$ -decay, without the production of Auger cascades. This experimental result demonstrates that in this oxide, without additional Auger electron holes trapped at Cd beyond the single hole at the acceptor impurity level, all  $^{111}\text{Cd}$  probes filled the impurity level ( $q=1-$ ) at all temperatures, aside from the time required to reach this stable state. This supports the conclusion that the EC is a necessary condition for observing the final stable

values of  $\text{HFI}_d$  in this oxide. However, it is illogical to rely on the absence of “aftereffects” when using  $^{111m}\text{Cd}$  to determine whether the EC is a necessary condition for observing dynamic HFIs. In this case, there are no dynamic HFIs because of the long lifetime of the  $11/2^+$  state, not due to the absence of the EC. As stated in Ref. [16], without EC, any probe impurity that introduces acceptor or donor states (in semiconductors and insulators) and whose ionization changes the EFG should exhibit a time-dependent HFI, as long as the lifetime of the dynamic process (such as the ionization of electron holes or donor electrons, respectively) exceeds the lifetime of the nuclear levels that feed the  $\gamma_1$  state and the state itself.

The current electronic interpretation of  $\text{HFI}_d$  differs entirely from the structural defect scenario proposed by Penner *et al.*, as discussed in Sec. II. B and C. Is it possible to have more than one electron hole as a final state for  $\text{HFI}_d$ ? For this to occur, the Fermi energy must be very low, and these charge states should have a lower formation energy than the  $\text{Al}_2\text{O}_3:\text{Cd}^0$  state. To verify this, we calculated the formation energy for two holes ( $\text{Al}_2\text{O}_3:\text{Cd}^{1+}$ ). As shown in Fig. 8(a), this situation is indeed energetically unfavorable for the previously mentioned Fermi levels. The same trend, gradually, applies to any system between  $\text{Al}_2\text{O}_3:\text{Cd}^0$  and  $\text{Al}_2\text{O}_3:\text{Cd}^{1+}$ .

#### IV. BÄVERSTAM-OTHAZ ANALYSIS OF THE EXPERIMENT AND INTEGRAL DISCUSSION

We present here the results of applying the BO approach to the TDPAC experimental data reported by Penner *et al.* [14]. Figure 9 shows how well Eq. (3) fits the selected  $R(t)$  spectra measured at 4 K, 293 K, and 910 K. As expected, two hyperfine interactions are required to account for the spectra at each temperature, with coupling constants and an asymmetry parameter of zero identical to those reported for  $\text{HFI}_u$  and  $\text{HFI}_d$  in Ref. [14]. In our case, both interactions were considered as single-crystalline. The  $V_{33}$  orientation for both interactions was determined parallel to the [001] crystal axis, as reported by Penner *et al.* for  $\text{HFI}_u$ . The fitted populations are similar to those in Penner's analysis. However, the frequency distributions, especially that of  $\text{HFI}_d$  to a greater extent, are notably lower because a dynamic perturbation factor is used instead of the static perturbation factors in Ref. [14], as required by the L approach. It is worth noting that the BO approach provides an excellent fit across the entire spectrum, particularly within the first 5-15 ns. In contrast, a static perturbation factor cannot accurately fit these short times.

As discussed in Sec. II, applying the BO approach to a single experimental spectrum enables the determination of the final EFG for  $HFI_u$  and  $HFI_d$ , as well as the atomic recovery constant  $\lambda_g$  and the relaxation constant  $\lambda_r$ , for each interaction at a given temperature.

Figure 10 compares the relaxation rate  $\Gamma_r$  for  $HFI_u$  as a function of temperature, derived from Penner *et al.*'s data using the L approach, with  $\lambda_g$  (shown in red) obtained here via the BO approach from the  $R(t)$  spectra in Fig. 9. As observed, Fig. 10 shows strong agreement between the results from both approaches at these three representative temperatures. Having identified  $\Gamma_r$  with  $\lambda_g$  (the inverse of the electron hole lifetime  $\tau_g$ ), its temperature dependence indicates an increase in electron availability at higher temperatures. At very low temperatures, this is likely due to increased electron conductivity. The different slopes in the  $\Gamma_r$  dependence on  $T$  (below 100 K and above 750 K) are examined in detail through two transport models for electrons in Ref. [14]. The excellent agreement shown in Fig. 10 provides the first evidence of the equivalence between the BO and L approaches, as  $\Gamma_r$  and  $\lambda_g$  represent the same physical quantity but are obtained through very different methods.

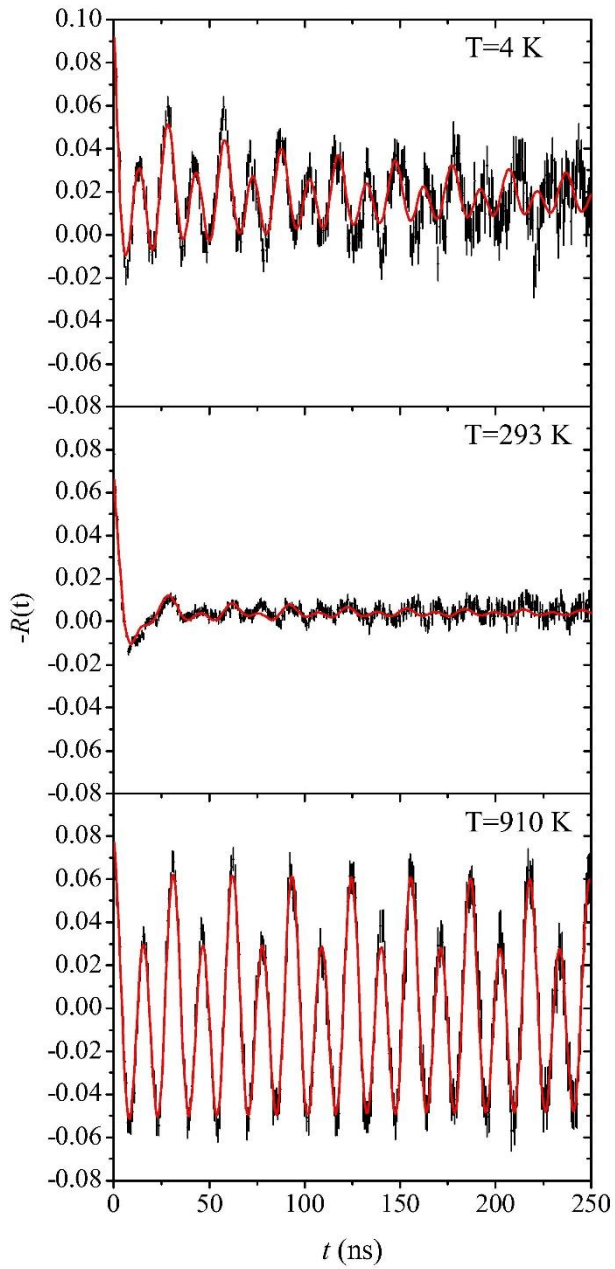


**FIG. 9.**  $R(t)$  spectra measured at 4 K, 293 K, and 910 K were analyzed using the BO perturbation factor in the *TDPAC* fitting program [38], modified for single crystals. Black points and error bars represent the experimental data reported by Penner *et al.* [14], while the red lines show the results of our least-squares fit of Eq. (3) to the data.

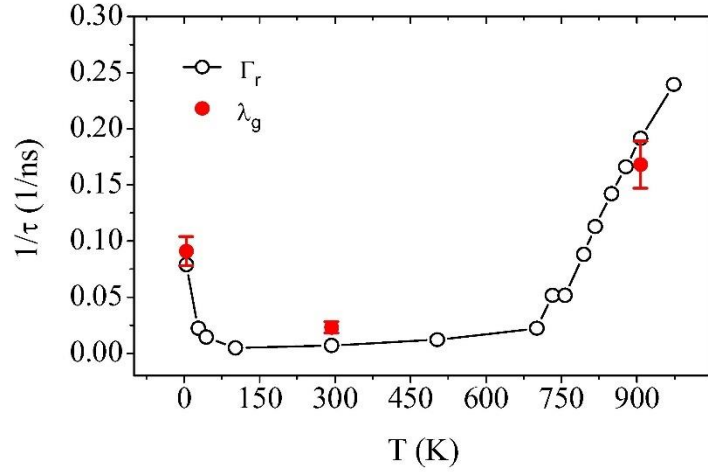


**FIG. 10.** Comparison of the relaxation rate  $\Gamma_r$  (open circles) as a function of measurement temperature, obtained by Penner *et al.* applying the L approach to HFI<sub>u</sub> [14], and the atomic recovery constant  $\lambda_g$  (the inverse of the electron holes lifetime  $\tau_g=1/\lambda_g$ ) determined with the BO approach by fitting Eq. (3) to selected experimental  $R(t)$  spectra reported in Ref. [14] at 4 K, 293 K, and 910 K (red filled circles).

In Table I, we present the dynamic parameters  $\lambda_g$  and  $\lambda_r$  for both HFI<sub>u</sub> and HFI<sub>d</sub>, along with their populations and the electron hole lifetime  $\tau_g$  for each interaction. These values were determined by fitting the BO perturbation factor to the  $R(t)$  spectra shown in Fig. 9.

T (K)	HFI <sub>u</sub>				HFI <sub>d</sub>			
	$f$ (%)	$\lambda_g$ (MHz)	$\lambda_r$ (MHz)	$\tau_g$ (ns)	$f$ (%)	$\lambda_g$ (MHz)	$\lambda_r$ (MHz)	$\tau_g$ (ns)
4	48 (1)	91 (13)	2.2 (4)	11 (2)	52 (1)	22 (6)	39 (5)	45 (12)
293	18 (1)	23 (5)	109 (8)	43 (9)	82 (1)	48 (14)	283 (25)	20 (6)
910	90 (1)	168 (21)	4.7 (7)	6 (1)	10 (1)	192 (23)	8 (2)	5 (1)

**TABLE I.** Dynamic hyperfine parameters  $\lambda_g$ ,  $\lambda_r$ , and the fraction of  $^{111}\text{Cd}$  probes detecting each interaction, HFI<sub>u</sub> and HFI<sub>d</sub>, determined by applying the BO approach to the three selected  $R(t)$  spectra shown in Fig. 9. The calculated lifetime,  $\tau_g=1/\lambda_g$ , of the electron holes (see text) is also displayed.

As mentioned in Sec. II.C, the  $\lambda_r$  parameter is associated with  $\Delta\delta$  ( $= \delta_i$ ) of the L approach. At this point, we must mention that the value  $\Delta\delta^u = 90$  MHz (of HFI<sub>u</sub>) reported in Ref. [14] was determined for  $n = 1$  when using Eq. (6), even though the single crystal orientation in the experimental setup requires using  $n = 2$ . Therefore,  $\Delta\delta^u = 45$  MHz (HWHM) and  $\Delta\nu_Q^u = 10$  MHz are the correct values that fit Eq. (6) perfectly, with  $n = 2$ , to the experimental data shown in Fig. 3 of Ref. [14]. In the L approach, it is necessary to have a complete set of measurements as a function of temperature to determine these kinds of “average” values for  $\delta_i^u$  and  $\nu_{Qi}^u$ , representing the entire temperature range. Hence,  $\delta_i^u = 45$  MHz represents a wide range of initial EFGs’ distributions. In comparison, the BO approach yields  $\lambda_r$  values across temperatures from 2.2 to 109 MHz (average of 55.6), further demonstrating the agreement between the two methods.

By leveraging the BO approach’s ability to determine all the dynamic parameters listed in Table I for both interactions and temperatures (including the hyperfine parameters not shown), its equivalence with the L approach, and combining these results with the *ab initio* predictions of the EFG as a function of the impurity’s charge state shown in Fig. 5 and Fig. 7, we can describe the electronic behavior of the dilute system during the dynamic regime across the entire temperature range.

We found that the maximum number of dynamic electron holes in HFI<sub>u</sub> is lower than in HFI<sub>d</sub> at all temperatures. It ranges from 0.03 (at both high and low temperatures) to one hole (at 293 K) for HFI<sub>u</sub>, and from 0.05 (at high temperatures) to at least five holes (at 293 K) for HFI<sub>d</sub>. These quantities of electron holes were determined by correlating the range of the initial EFGs with the corresponding charge states  $q$ . In turn, the initial EFGs’ range at each temperature was calculated as  $EFG_i \pm \delta_i$ , considering  $\delta_i = \lambda_r$  and  $EFG_i \approx EFG_f$  within the equivalence.

As seen in Table I, at 293 K (where the  $R(t)$  spectra are highly damped, and the ECAE are stronger), electronic availability is very low. At this temperature, before the  $\gamma_1$  emission, the deepest electron holes at the probe atoms are ionized in two different ways. When  $\gamma_1$  is emitted, 18 % of probe atoms (HFI<sub>u</sub>) have all their electron holes ionized, except for one, while 82 % of the probes (HFI<sub>d</sub>) retain at least five electron holes. This is the primary physical difference between the two HFIs, not their final electronic state, which depends on the availability of electrons at each temperature. Now, let us describe the behavior of electron holes in the dynamic regime at this temperature. As shown in Table I, HFI<sub>u</sub> takes longer than HFI<sub>d</sub> to fill fewer electron holes. Remember that  $\tau_g$  starts when  $\gamma_1$  is emitted and ends when the dynamic regime terminates. Since deeper empty states must be filled first because this reduces the

system's energy, HFI<sub>d</sub> uses the first, let's say, 15 ns to fill four electron holes, then five ns to fill the remaining 0.65 holes, totaling 20 ns to reach the final stable charge state  $q=0.65$  (leaving 0.35 unoccupied electron holes). On the other hand, during these first 15 ns, HFI<sub>u</sub> does not fill any electron holes because its four deeper electron holes are already filled before the  $\gamma_1$  emission. When HFI<sub>d</sub> begins to fill the last 0.65 holes, HFI<sub>u</sub> starts filling the remaining electron hole, taking five ns to fill 0.65 of its hole (like HFI<sub>d</sub>), and an additional 23 ns to fill the remaining 0.35 hole, reaching the  $q=1^-$  final stable charge state.

At 4 K, electron availability decreases further. Despite this,  $\lambda_r$  drops significantly - by a factor of 50 for HFI<sub>u</sub> and 7 for HFI<sub>d</sub> - restoring the spectral anisotropy, an effect previously observed in TDPAC experiments on other oxides doped with <sup>111</sup>In ions [11, 12, 39-41]. At this temperature, the distribution of initial oscillating EFGs for HFI<sub>d</sub> is roughly 20 times wider than for HFI<sub>u</sub> (see  $\lambda_r$  in Table I). In this very low-temperature range, Penner *et al.* attribute the higher relaxation rates  $\Gamma_r$ , which indicate shorter hole lifetimes, to increased electron mobility resulting from carrier transport across localized states of the same energy, known as coherent tunneling [42]. In 11 ns, about half of the probes sensing HFI<sub>u</sub> fill 0.02 electron holes to complete the impurity level, whereas those sensing HFI<sub>d</sub> take three times longer to reach the  $q=0.9^-$  charge state by filling 0.4 electron holes. Considering the dynamic hyperfine parameters measured for HFI<sub>u</sub>, which produce an almost undamped contribution and are sensed by only half the probes, the damping observed in the  $R(t)$  spectrum at this temperature is due to HFI<sub>d</sub>.

At high temperatures ( $T=910$  K), the two interactions are similar because HFI<sub>d</sub> tends toward the most populated HFI<sub>u</sub>. Increased electron availability due to thermal effects (a high Fermi energy) ensures that 90% of <sup>111</sup>Cd probes fill the impurity level during the dynamic process, leaving the remaining probes with 0.05 electron holes. For the same reason, both interactions have very low  $\lambda_r$  values because of a narrow range of initial EFGs (i.e., low variation in initial electronic configurations) and very small fractions of initial electron holes (0.03-0.05 for HFI<sub>u</sub> and 0.1 for HFI<sub>d</sub>) during the dynamic regime (very close to the  $q=1^-$  charge state). Accordingly, at this temperature, the hole lifetimes  $\tau_g$  for both interactions are also very short, with 10% of the probes (HFI<sub>d</sub>) filling quickly ( $\tau_g^d = 5$  ns) the small fraction of dynamic electron holes up to a charge state  $q=0.95^-$ . One nanosecond later ( $\tau_g^u = 6$  ns), 90% of the probes (HFI<sub>u</sub>) complete filling of the impurity level, thanks to the favorable energetic situation for the  $q=1^-$  charge state [see Fig. 8(a)] due to the high Fermi energy at this temperature and the lower fraction of initial electron holes (0.03) trapped at the <sup>111</sup>Cd probes sensing HFI<sub>u</sub>.

From this electronic behavior, we can conclude that as the number of electron holes during the dynamic regime (and thus the range of oscillating initial EFGs) increases, a larger fraction of them becomes involved in producing the final EFG<sub>f</sub>. This applies to HFI<sub>d</sub> transitioning from high to intermediate temperatures. Conversely, when the initial number of electron holes is small (e.g., at high temperature for HFI<sub>d</sub>), the range of oscillating initial EFGs becomes limited, and the final EFG<sub>f</sub> tends to match that measured for HFI<sub>u</sub> (which is with the impurity level filled).

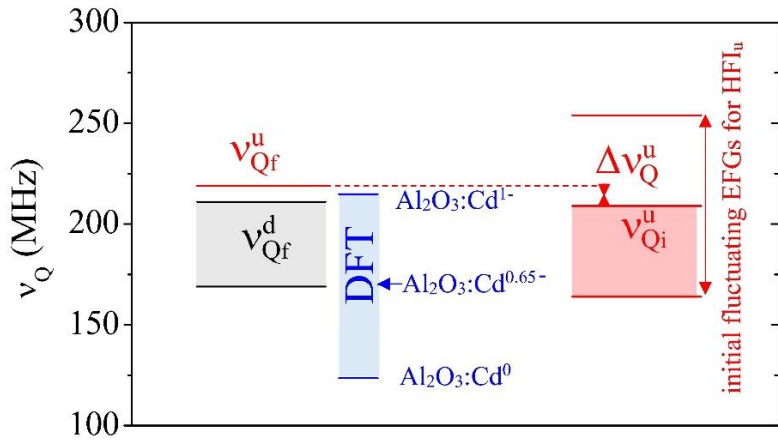


**FIG. 11.** Comparison between the final stable coupling constant  $v_{Q_f}$  reported by Penner *et al.* [14] in the 4-973 K temperature range for both hyperfine interactions HFI<sub>u</sub> and HFI<sub>d</sub> (on the left), along with *ab initio* predictions for  $v_Q$  as a function of the charge states of the Cd atom (middle). On the right, the average value (across all measured temperatures) of the initial fluctuating coupling constant,  $v_{Q_i}^u$ , and its distribution width as determined by the L approach (see text) are shown for HFI<sub>u</sub>. The difference  $\Delta v_Q^u$  between  $v_{Q_f}^u$  and  $v_{Q_i}^u$  is also shown on this side.

Let's now present a graphical summary and discuss the proposed scenario for the origin of the EFG in more detail, including the initial stages during the dynamic regime and the final stable state after fluctuations cease, for HFI<sub>u</sub> and HFI<sub>d</sub> within the framework of the BO and L approaches and *ab initio* predictions. Figure 11 shows, on the left, the experimental EFGs observed for HFI<sub>u</sub> and HFI<sub>d</sub> across the entire temperature range (expressed for comparison purposes in terms of the coupling constant  $v_Q$ , see Sec. II); in the middle, the *ab initio*

predictions of the EFG at the Cd site for charge states from  $q=0$  to  $q=1-$ ; and on the right, the initial mean value  $\nu_{Qi}^u$  and its distribution half-width  $\delta_i^u$ , as determined by Penner *et al.* applying the L approach. In effect, as described in Sec. III.B, the predicted EFG for  $q=1-$  perfectly matches the experimental EFG of HFI<sub>u</sub> (its final stable EFG), and the range of the experimental EFGs (the final stable ones) for HFI<sub>d</sub> over the entire temperature range corresponds to predictions between  $q=0.65-$  and  $q=1-$ , which represent 0.35 electron holes and no trapped holes at the Cd atom, respectively. Predicted EFGs that simulate more than one electron hole do not match the experimental values reported in Ref. [14], falling significantly below this range. For example, with two electron holes ( $q=1+$ ), the predicted value is  $V_{33}=4.23 \times 10^{21} \text{ V/m}^2$  (84.9 MHz). Refer to Fig. 5, Fig. 7, and Fig. 11 for comparison. Additionally, this situation is energetically unfavorable [see the green line in Fig. 8(a)]. The same scenario occurs when more than one electron is added to the system, predicting  $V_{33}=11.10 \times 10^{21} \text{ V/m}^2$  and  $V_{33}=11.43 \times 10^{21} \text{ V/m}^2$  for  $q=1.1-$  and  $q=1.2-$ , respectively, exceeding the HFI<sub>u</sub> experimental value (see Figs. 5 and 6). Similarly, for these charge states, the defect formation energy begins to rise [dashed blue line in Fig. 8(a)], leading once again to an unfavorable situation.

In Fig. 11 (on the right), due to the uncertainty of the EFG sign in a standard TDPAC experiment, we assume the positive sign of  $\nu_{Q_f}^u$ , given by the *ab initio* calculation. Since Eq. (6) is insensitive to the  $\Delta\nu_Q^u$  sign, we select the smaller value for  $\nu_{Qi}^u$  between the two options from the determination of  $\Delta\nu_Q^u = \nu_{Q_f}^u - \nu_{Qi}^u$ , because the other would lead to an initial positive value  $\nu_{Qi}^u$  larger than  $\nu_{Q_f}^u$ , which in the calculations corresponds to the addition of more than one electron. This is not only energetically unfavorable but would also yield unphysical initial EFGs, arising from the addition of electrons to the conduction band rather than from the presence of electron holes created by the EC. For the same reason, we have only highlighted the initial EFGs region in this figure corresponding to  $\nu_{Qi}^u - \delta_i^u$ , since the majority of the other side of the frequency distribution (above  $\nu_{Q_f}^u$ ) appears unphysical in this case. As shown, the range of initial EFGs that originate the dynamic regime between  $\nu_{Qi}^u$  and  $\nu_{Qi}^u - \delta_i^u$  (shaded pink region on the right side of Fig. 11) using the L approach matches perfectly with the range of experimental final EFGs for HFI<sub>d</sub> across the entire measurement temperature range (shaded grey region on the left side of Fig. 11). This agreement strongly supports the interpretation of HFI<sub>d</sub>'s origin, which is accurately reflected by the charge states between  $q=1-$  and  $q=0.65-$ . On the other hand, the range of initial EFGs for HFI<sub>u</sub>, which we note as an average value across all measurement temperatures obtained by Penner *et al.* within the L approach (with a distribution half-width of about 45 MHz), is roughly the same magnitude as that determined in the BO

approach (using  $\lambda_r$ ) at intermediate temperatures for this interaction (see Table I), where the dynamic effects are more pronounced. Assuming the equivalence between the two approaches is valid, which requires that  $EFG_i \approx EFG_f$ , the range of the initial EFGs for  $HFI_u$  can be determined from the experimental final  $EFG_f$  to lower values. Thus, the range of initial EFGs determined by the BO approach at RT (with a spread of  $\lambda_r = 109$  MHz) corresponds to the range of predicted EFGs between the situation in which the impurity level is filled and that of having one electron hole (see Fig. 11, middle, shaded light blue region). A similar situation was observed with  $\text{SnO}:\text{In}^{111}(\rightarrow \text{Cd}^{111})$ , where the dynamic regime resulted from charge-state fluctuations involving up to one electron hole [16]. In our system, the  $\lambda_r$  values for  $HFI_u$  at high and very low temperatures are minimal, indicating that the possible electronic configurations during the dynamic regime correspond to a narrow charge-state range very close to the  $q=1$ -state (with less than 0.05 electron holes).

In the case of  $HFI_d$ , the L approach was not used in Ref. [14]. However, the BO approach and the integral analysis presented here enable the determination of the initial EFGs range at each temperature for this interaction. At low temperatures, an initial EFG range (measured from  $EFG_i = 200$  MHz with a spread related to  $\lambda_r = 39$  MHz) correlates with having up to about 0.45 holes during the dynamic process, and at high temperature up to 0.05 electron holes, corresponding to  $\lambda_r = 8$  MHz (see Fig. 5 and 7, and the recent discussion). At RT, where the dynamic effect is stronger, predictions become more challenging. An enormous  $\lambda_r$  value of 280 MHz covers all possible decreasing EFG values, indicating that at least five electron holes are involved during the dynamic regime. Fig. 8(a) shows that this situation is energetically very unfavorable unless an external factor shifts the Fermi energy deep into the valence band. In our case, this extreme scenario arises from Auger cascades caused by  $^{111}\text{In}$  EC nuclear decay, followed by electronic relaxation and recombination at the  $^{111}\text{Cd}$  atom, along with limited electron availability and/or mobility at this temperature in the current dilute semiconductor.

Finally, we highlight the importance of establishing the equivalence between the two approaches. This allows us to identify  $\lambda_r$  with the distribution half-width of the initial EFGs that produce the dynamic interaction and, therefore, determine the range of initial oscillating EFGs for each temperature and both hyperfine interactions using the BO model. Comparing these experimental quantities with the *ab initio* predictions enabled the extraction of key insights into the electronic configurations involved in this complex doped system, both during and after the dynamic regime. On the other hand, the straightforward determination of the hole lifetime's temperature dependence using the BO approach in  $^{111}\text{In}$ -doped materials or other

diluted systems that exhibit this *on-off* dynamic regime can be a powerful tool for studying conduction and transport properties in such systems.

## V. CONCLUSIONS

We demonstrated, through a comprehensive combined *ab initio*/DFT and double-approach experimental study, the conditions needed to establish the equivalence between the perturbation factors of very different methods proposed by Bäverstam *et al.* and Lupascu *et al.* for addressing time-dependent *on-off* hyperfine interactions, such as those caused by the electron-capture decay “aftereffects” (ECAE) phenomenon.

For the diluted semiconductor studied here, ( $^{111}\text{In} \rightarrow$ ) $^{111}\text{Cd}$ -doped  $\alpha\text{-Al}_2\text{O}_3$ , these conditions were satisfied. This equivalence enabled us to apply the BO approach to determine the range of initial EFGs generated by the dynamic electronic relaxation and recombination process, which, in this case, follows the electron capture that initiates the nuclear decay of  $^{111}\text{In}$  ions implanted in single crystals of  $\alpha\text{-Al}_2\text{O}_3$ . This analysis was applied to both experimentally observed hyperfine interactions and at each measured temperature. If the L approach is used alone, it requires a series of TDPAC measurements at different temperatures to determine the initial EFGs, but averages them over all temperatures. Of course, the final stable EFG reached for each interaction at each measured temperature is precisely determined with both approaches. Until now, the relaxation constant  $\lambda_r$  of the BO model has been treated as a phenomenological parameter that describes the damping strength of TDPAC spectra caused by rapid, random EFG fluctuations during the dynamic phase of the ECAE phenomenon. However, this analysis found it to be half the width of the distribution of initial fluctuating EFGs.

On the other hand, the strong agreement between the experimental recovery constant  $\lambda_g$  in the BO model and the relaxation rate  $\Gamma_r$  obtained independently from the simulations of the L approach at different temperatures for  $\text{HFI}_u$ , both representing the inverse of the lifetime  $\tau_g$  of those electron holes involved in the dynamic process that will finally be ionized, strongly supports the equivalence of both perturbation factors.

The strong agreement between the EFG predictions from *ab initio* calculations, which take into account the existence of different charge states of the Cd impurity caused by trapped electron holes, and the experimental *final* stable EFGs measured by the  $^{111}\text{Cd}$  probe for both

interactions after the dynamic process, enabled us to connect the fluctuating *initial* EFGs observed experimentally with the various fluctuating electronic configurations (holes) that cause them through this integral analysis.

First, we demonstrated that the experimental final EFG of  $\text{HFI}_u$  corresponds to the charge state  $q = 1-$ , indicating that the impurity level is filled. We showed that the slight linear decrease in this EFG with increasing temperature results from strong nonlinear thermal lattice expansion, rather than from an electronic effect, thereby allowing us to distinguish between structural and electronic sources.

Conversely, the experimental *final* EFG of  $\text{HFI}_d$  varies notably with temperature. These EFGs were correlated with the electronic configurations adopted by the probe atom at each temperature, depending on the host's electron availability and mobility. These configurations range from 0 to 0.35 electron holes trapped at the probe impurity. We showed that the significant increase in the EFG of  $\text{HFI}_d$  with rising temperature results from the accumulation of more negative charge closer to the (001) plane than near the [001] crystalline axis, as the degree of electron hole ionization increases.

The agreement shown in our analysis between these temperature-dependent *final stable* EFGs reached by  $\text{HFI}_d$  and the *initial* EFGs that create the dynamic regime for  $\text{HFI}_u$  (determined independently using the L approach), within our *ab initio* calculations of the EFG, supports the existence of these fractional charge states of the impurity associated with a temperature-dependent Fermi energy. This Fermi energy also fluctuates during the dynamic regime in a region very close to the top of the impurity level.

The application of the BO approach enabling the overall analysis of  $\tau_g$ , now for *both* interactions and *each* measuring temperature, showed a good correlation with the variation of the electron availability at high and intermediate temperatures, and with the availability and mobility of electrons for very low temperatures in which the anisotropy of the TDPAC signal is recovered, recovery assigned to an increase of carrier conductivity probably due to tunneling effects. The  $\tau_g$  values obtained for each interaction enabled us to describe and quantify how the empty states (trapped electron holes) at  $^{111}\text{Cd}$  probes are filled during the dynamic process across the three selected temperature ranges. At high temperatures, the small number of trapped electron holes when  $\gamma_1$  is emitted lives around five ns, while at room temperature, between 20-40 ns (when one or more than five holes are trapped at  $^{111}\text{Cd}$  probes sensing  $\text{HFI}_u$  and  $\text{HFI}_d$ , respectively). At very low temperatures, those holes associated with  $\text{HFI}_u$  live for 11 ns. In comparison, those associated with  $\text{HFI}_d$  live for 45 ns because of the larger number of empty

states involved in the initial fluctuating EFGs during the dynamic regime of this interaction. It was shown that the maximum lifetime of the trapped electron holes in this oxide is about 45 ns. This occurs at very low temperatures for  $HFI_d$ , and at RT for  $HFI_u$ . It became clear that the reason dynamic hyperfine interactions were not observed in TDPAC experiments in  $\alpha\text{-Al}_2\text{O}_3$  using  $^{111m}\text{Cd}$  as a probe is this short recovery time relative to the very long lifetime of the state emitting the  $\gamma_1$ -ray in this probe (48.6 min), and not the absence of an EC, which would promote the formation of extra electron holes.

Regarding the range of the initial fluctuating EFGs, it was determined for  $HFI_u$  by the BO (through  $\lambda_r$  at each temperature) and L (through  $\delta_i$  as an average) approaches, with good agreement between the two methods. These results were correlated with *ab initio* predictions of the presence of, e.g., up to 1 electron hole at RT. For  $HFI_d$ , only the BO approach was applied, showing that at least 5 electron holes are trapped at the  $^{111}\text{Cd}$  atom at RT when the dynamic regime begins. Strictly speaking, the BO approach alone provides only the half-width of the initial fluctuating EFG distribution, not its range. However, this range was determined within our proposed integrated scenario, noting that the EFG distribution is centered on its upper tail for this impurity-host system, which also matches the final stable EFG when the system is close to the conditions of equivalence.

We addressed the apparent contradiction that a spectrum from a dynamic process that never ends, as evidenced by continuous damping, displays a well-defined EFG, even though a stable final EFG<sub>f</sub> does not exist. At least when the equivalence conditions are met, as  $EFG_i = EFG_f$ , it is  $EFG_i$  that determines the well-defined shape of the spectrum. In this case, the perturbation factor of BO and L approaches takes the same form: a static  $G_{22}(t)$  damped by an exponential term. These findings also support our proposal that EFG<sub>f</sub> participates among the initial fluctuating EFGs, with the highest probability.

In summary, this detailed experimental and theoretical DFT study allowed us to identify, at each temperature, the initial electronic configurations near the probe nucleus that the system fluctuates between to produce the observed dynamic HFIs. It also established the final stable configurations, supporting and confirming the physical scenario underlying both the BO and L approaches used to model the ECAE phenomenon in diluted semiconductors and insulators. The methodology developed in this work can certainly be applied to future studies aimed at understanding transport and conduction properties in these materials.

## ACKNOWLEDGEMENTS

CONICET and UNLP partially supported this work under Research Grants No. PIP0901 and No. 11/X1004, respectively, as well as by the Deutsche Forschungsgemeinschaft (DFG, German Research Foundation) under Grant No. VI 77/3Y1. This research used the computational facilities of the Physics of Impurities in Condensed Matter group at IFLP and the Department of Physics (UNLP). M.R. is grateful to Professors Dr. A.G. Bibiloni and Dra. C.P. Massolo for pioneering and encouraging discussions on the ECAE phenomenon, and G.N.D. and M.R. gratefully acknowledge Professor Dr. A.F. Pasquevich for fruitful discussions on the time-dependent perturbation factor. Insightful talks about defect formation energy DFT calculations by Prof. Dra. L.V.C. Assali are kindly acknowledged. G.N.D. and M.R. are members of CONICET, Argentina.

\* Contact author: [darriba@fisica.unlp.edu.ar](mailto:darriba@fisica.unlp.edu.ar)

† Contact author: [renteria@fisica.unlp.edu.ar](mailto:renteria@fisica.unlp.edu.ar)

## REFERENCES

- [1] T. Dietl, A Ten-Year Perspective on Dilute Magnetic Semiconductors and Oxides, *Nat. Mater.* **9**, 965 (2010)
- [2] R. J. Green, T. Z. Regier, B. Leedahl, J. A. McLeod, X. H. Xu, G. S. Chang, E. Z. Kurmaev, and A. Moewes, Adjacent Fe-Vacancy Interactions as the Origin of Room Temperature Ferromagnetism in  $(In_{1-x}Fe_x)_2O_3$ , *Phys. Rev. Lett.* **115**, 167401 (2015).
- [3] X. Cai, F. P. Sabino, A. Janotti, and S-H Wei, Approach to achieving a *p*-type transparent conducting oxide: Doping of bismuth-alloyed  $Ga_2O_3$  with a strongly correlated band edge state, *Phys. Rev. B* **103**, 115205 (2021)
- [4] J. Zhi, M. Zhou, Z. Zhang, O. Reiser, and F. Huang, Interstitial Boron-Doped Mesoporous Semiconductor Oxides for Ultratransparent Energy Storage, *Nat. Commun.* **12**, 445 (2021).
- [5] S. Chaturvedi and U. V. Waghmare, Origin of ferromagnetism in a two-dimensional dilute magnetic semiconductor  $h\text{-Co}_x\text{Zn}_{1-x}\text{O}$ , *Phys. Rev. B* **112**, 094437 (2025).
- [6] A. G. Bibiloni, C. P. Massolo, J. Desimoni, L. A. Mendoza-Zélis, F. H. Sánchez, A. F. Pasquevich, L. Damonte, and A. R. López-García, Time-Differential Perturbed-Angular-Correlation Study of Pure and Sn-Doped  $In_2O_3$  Semiconductors, *Phys. Rev. B* **32**, 2393 (1985).
- [7] C. P. Massolo, J. Desimoni, A. G. Bibiloni, L. A. Mendoza-Zélis, L. C. Damonte, A. R. Lopez-García, P. W. Martin, S. R. Dong, and J. G. Hooley, Aftereffect Investigations in Mixed-Valence Indium Chlorides, *Phys. Rev. B* **34**, 8857 (1986).

[8] W. Bolse, M. Uhrmacher, and J. Kesten, The EFG of the In-O-Bond  $\text{In}_2\text{O}_3$ ,  $\text{AgO}$  and  $\text{Ag}_2\text{O}$ , *Hyperfine Interact.* **35**, 931 (1987).

[9] K. Asai, F. Ambe, S. Ambe, T. Okada, and H. Sekizawa, Time-Differential Perturbed-Angular-Correlation Study of Hyperfine Interactions at  $^{111}\text{Cd}(\leftarrow ^{111}\text{In})$  in  $\alpha\text{-Fe}_2\text{O}_3$ , *Phys. Rev. B* **41**, 6124 (1990).

[10] A. Bartos, K. P. Lieb, A. F. Pasquevich, and M. Uhrmacher, Scaling of the Electric Field Gradient of  $^{111}\text{Cd}$  Impurities in the Bixbyite Oxides of Y, Sc, Dy and Yb, *Phys. Lett. A* **157**, 513 (1991).

[11] D. Lupascu, S. Habenicht, K.-P. Lieb, M. Neubauer, M. Uhrmacher, and T. Wenzel, Relaxation of Electronic Defects in Pure and Doped  $\text{La}_2\text{O}_3$  Observed by Perturbed Angular Correlations, *Phys. Rev. B* **54**, 871 (1996).

[12] S. Habenicht, D. Lupascu, M. Uhrmacher, L. Ziegeler, and K.-P. Lieb, PAC-Studies of Sn-Doped  $\text{In}_2\text{O}_3$ : Electronic Defect Relaxation Following the  $^{111}\text{In}(\text{EC})^{111}\text{Cd}$ -Decay, *Z. Phys. B* **101**, 187 (1996).

[13] S. Habenicht, D. Lupascu, M. Neubauer, M. Uhrmacher, K. P. Lieb, and the ISOLDE-Collaboration, Doping of Sapphire Single Crystals with  $^{111}\text{In}$  and  $^{111}\text{Cd}$  Detected by Perturbed Angular Correlation, *Hyperfine Interact.* **120**, 445 (1999).

[14] J. Penner and R. Vianden, Temperature Dependence of the Quadrupole Interaction for  $^{111}\text{In}$  in Sapphire, *Hyperfine Interact.* **158**, 389 (2004).

[15] G. N. Darriba, E. L. Muñoz, A. W. Carbonari, and M. Rentería, Experimental TDPAC and Theoretical DFT Study of Structural, Electronic, and Hyperfine Properties in  $(^{111}\text{In} \rightarrow)^{111}\text{Cd}$ -Doped  $\text{SnO}_2$  Semiconductor: Ab Initio Modeling of the Electron-Capture-Decay After-Effects Phenomenon, *J. Phys. Chem. C* **122**, 17423 (2018).

[16] G. N. Darriba, E. L. Muñoz, D. Richard, A. P. Ayala, A. W. Carbonari, H. M. Petrilli, and M. Rentería, Insights into the Aftereffects Phenomenon in Solids Based on DFT and Time-Differential Perturbed  $\gamma$ - $\gamma$  Angular Correlation Studies in  $^{111}\text{In}(\rightarrow^{111}\text{Cd})$ -Doped Tin Oxides, *Phys. Rev. B* **105**, 195201 (2022).

[17] U. Bäverstam, R. Othaz, N. de Sousa, and B. Ringström, After-Effects in the Decay of  $^{75}\text{As}$  and  $^{197\text{m}}\text{Hg}$ , *Nucl. Phys. A* **186**, 500 (1972).

[18] M. Iwatschenko-Borho, W. Engel, H. Foettinger, D. Forkel, F. Meyer, and W. Witthuhn, In-Beam Studies of Defect Cascades in Metals, *Nucl. Instrum. Methods Phys. Res. B* **7-8**, 128 (1985).

[19] G. K. H. Madsen, P. Blaha, K. Schwarz, E. Sjöstedt, and L. Nordström, Efficient Linearization of the Augmented Plane-Wave Method, *Phys. Rev. B* **64**, 195134 (2001).

[20] H. Frauenfelder and R. M. Steffen, *Alpha-, Beta-, and Gamma-Ray Spectroscopy*, K. Seigbahn, Vol. 2 (North-Holland Publishing Co., Amsterdam, Netherland, 1968).

[21] E. N. Kaufmann and R. J. Vianden, The Electric Field Gradient in Noncubic Metals, *Rev. Mod. Phys.* **51**, 161 (1979).

[22] G. Schatz and A. Weidinger, *Nuclear Condensed Matter Physics: Nuclear Methods and Applications* (Wiley, Chichester, England, 1996).

[23] G. N. Darriba, R. Faccio, P.-D. Eversheim, and M. Rentería, Insights on the Relevance of DFT+ $U$  Formalism for Strongly Correlated Ta  $d$  Electrons Probing the Nanoscale in Oxides:

Combined Time-Differential Perturbed  $\gamma$ - $\gamma$  Angular Correlation Spectroscopy and *Ab Initio* Study in  $^{181}\text{Hf}(\rightarrow ^{181}\text{Ta})$ -Implanted  $\alpha$ - $\text{Al}_2\text{O}_3$  Single Crystal, *Phys. Rev.* **108**, 245144 (2023).

- [24] A. Abragam and R. V. Pound, Influence of Electric and Magnetic Fields on Angular Correlations, *Phys. Rev.* **92**, 943 (1953).
- [25] A. F. Pasquevich and M. Rentería, in *Defects and Diffusion Studied Using PAC Spectroscopy*, edited by H. Jaeger and M.O. Zacate (Trans Tech Publications Ltd, Zurich, Switzerland, 2011), pp. 62-104, <https://main.scientific.net/book/defects-and-diffusion-studied-using-pac-spectroscopy/978-3-03813-516-6/ebook>.
- [26] H. Winkler and E. Gerdau,  $\gamma\gamma$ -Angular Correlations Perturbed by Stochastic Fluctuating Fields, *Z. Physik* **262**, 363 (1973).
- [27] H. Winkler,  $\gamma\gamma$  Angular correlations perturbed by randomly reorienting hyperfine fields, *Z. Physik A* **276**, 225 (1976).
- [28] M. Uhrmacher, M. Neubahuer, D. Lupascu, and K. P. Lieb, in Proceedings of the International Workshop “25th Anniversary of Hyperfine interactions at La Plata”, 1995 (Departamento de Física, UNLP, La Plata, 1995), p. 82.
- [29] F. Izumi, H. Asano, H. Murata, and N. Watanabe, Rietveld Analysis of Powder Patterns Obtained by TOF Neutron Diffraction Using Cold Neutron Sources, *J. App. Crystallogr.* **20**, 411 (1987).
- [30] G. N. Darriba, M. Rentería, H. M. Petrilli, and L. V. C. Assali, Site Localization of Cd Impurities in Sapphire, *Phys. Rev. B* **86**, 075203 (2012).
- [31] M. Lucht, M. Lerche, H.-C. Wille, Y. V. Shvyd’ko, H. D. Rüter, E. Gerdau, and P. Becker, Precise Measurement of the Lattice Parameters of  $\alpha$ - $\text{Al}_2\text{O}_3$  in the Temperature Range 4.5–250 K Using the Mössbauer Wavelength Standard, *J. Appl. Cryst.* **36**, 1075 (2003).
- [32] P. Blaha, K. Schwarz, G. Madsen, D. Kvasnicka, and J. Luitz, *WIEN2k, an Augmented Plane Wave Plus Local Orbitals Program for Calculating Crystal Properties* (Technical Universität, Wien, Austria, 2014).
- [33] P. E. Blöchl, Projector Augmented-Wave Method, *Phys. Rev. B* **50**, 17953 (1994).
- [34] J. P. Perdew, K. Burke, and M. Ernzerhof, Generalized Gradient Approximation Made Simple, *Phys. Rev. Lett.* **77**, 3865 (1996).
- [35] K. Schwarz, C. Ambrosch-Draxl, and P. Blaha, Charge Distribution and Electric-Field Gradients in  $\text{YBa}_2\text{Cu}_3\text{O}_{7-x}$ , *Phys. Rev. B* **42**, 2051 (1990).
- [36] P. Blaha, K. Schwarz, and P. H. Dederichs, First-Principles Calculation of the Electric-Field Gradient in Hcp Metals, *Phys. Rev. B* **37**, 2792 (1988).
- [37] P. Herzog, K. Freitag, M. Reuschenbach, and H. Walitzki, Nuclear Orientation of  $^{111m}\text{Cd}$  in Zn and Be and the Quadrupole Moment of the 245keV State, *Z. Physik A* **294**, 13 (1980).
- [38] A. P. Ayala, Program TDPAC, code developed to fit multiple-sites perturbation factors for static and dynamic hyperfine interactions in TDPAC experiments on polycrystalline samples, Ph.D. thesis, Universidad Nacional de La Plata, La Plata, Argentina, 1995, available on line at <https://sedici.unlp.edu.ar/handle/10915/2431>.
- [39] A. Lohstroh, M. Uhrmacher, P.-J. Wilbrandt, H. Wulff, L. Ziegeler, and K. P. Lieb, Electronic Relaxation in Indium Oxide Films Studied with Perturbed Angular Correlations, *Hyperfine Interact.* **159**, 35 (2004).

[40] E. L. Muñoz, D. Richard, A. W. Carbonari, L. A. Errico, and M. Rentería, PAC Study of Dynamic Hyperfine Interactions at  $^{111}\text{In}$ -Doped  $\text{Sc}_2\text{O}_3$  Semiconductor and Comparison with Ab Initio Calculations, *Hyperfine Interact.* **197**, 199 (2010).

[41] E. L. Muñoz, Ph.D. thesis, Universidad Nacional de La Plata, La Plata, Argentina, 2011, available on line at <http://sedici.unlp.edu.ar/handle/10915/2628>.

[42] K. W. Kehr, Empirical Information on Quantum Diffusion, *Hyperfine Interact.* **17**, 63 (1984).